Greenland ice sheet surface mass balance 1991–2000: Application of Polar MM5 mesoscale model and in situ data

Jason E. Box and David H. Bromwich

Polar Meteorology Group, Byrd Polar Research Center, Ohio State University, Columbus, Ohio, USA

Department of Geography, Atmospheric Sciences Program, Ohio State University, Columbus, Ohio, USA

Le-Sheng Bai

Polar Meteorology Group, Byrd Polar Research Center, Ohio State University, Columbus, Ohio, USA

Received 15 December 2003; revised 30 April 2004; accepted 12 May 2004; published 26 August 2004.

[1] The Polar Pennsylvania State University–National Center for Atmospheric Research Fifth-Generation Mesoscale Model (Polar MM5) regional climate model was run over the North Atlantic region for 1991–2000. We analyze 24-km output over the Greenland ice sheet to evaluate spatial and temporal variability of the surface mass balance and its subcomponents. The model output is compared with 3 years of automatic weather station (AWS) data from 17 sites to identify biases. Using the in situ data, we derive simple corrections for biases in melt energy and in water vapor fluxes from the surface and from blowing snow. The simulated accumulation rate is in agreement with AWS and snow pit observations. Estimates for runoff and the surface mass balance distribution over the ice sheet are produced using modeled melt volume and a meltwater retention scheme. From the decade investigated, the magnitude of interannual variability in surface mass balance components is tentatively established. The largest variability is concentrated along the ice sheet margin, where both accumulation and ablation rates are largest. The simulated interannual fluctuations suggest a large absolute variability, ± 187 km^3 yr^{-1} for total ice sheet surface mass balance. Variability in simulated equilibrium line altitude is suggestive of a dominance of thermal variability in the south with increasing importance of accumulation variability with increasing latitude. Empirical functions for the sensitivity of surface mass balance to temperature and precipitation anomalies are presented. The precise locations and regions of maximum and minimum surface energy and mass fluxes are suggested. Using an estimate for iceberg discharge and bottom melting, the total ice sheet mass balance is estimated be -78 km^3 yr^{-1}, producing 2.2 mm of eustatic sea level rise over the 1991–2000 decade and contributing 15% to the observed (1.5 mm yr^{-1}) global sea level rise. The more negative mass balance is attributed to including blowing-snow sublimation loss and to regional warming in the 1990s. *INDEX TERMS:* 1620 Global Change: Climate dynamics (3309); 1827 Hydrology: Glaciology (1863); 3360 Meteorology and Atmospheric Dynamics: Remote sensing; 3349 Meteorology and Atmospheric Dynamics: Polar meteorology; 4556 Oceanography: Physical: Sea level variations; *KEYWORDS:* Greenland ice sheet, mass balance, runoff

Citation: Box, J. E., D. H. Bromwich, and L.-S. Bai (2004), Greenland ice sheet surface mass balance 1991–2000: Application of Polar MM5 mesoscale model and in situ data, *J. Geophys. Res.*, *109*, D16105, doi:10.1029/2003JD004451.

1. Scientific Background

[2] Ice sheet mass balance plays an important role in global sea level and thermohaline circulation changes. Greenland ice sheet mass balance changes appear to have contributed several meters to sea level fluctuations since the last climatic optimum, 125,000 years ago [*Cuffey and Marshall*, 2000], and are expected to contribute to sea level rise under projected future global warming throughout this century [*Church et al.*, 2001]. However, Greenland ice sheet mass balance components are imprecisely known [*van der Veen*, 2002]. Therefore ranking the importance of the Greenland ice sheet in global ocean dynamics has been associated with large uncertainty. Contributing to this uncertainty, surface mass balance estimates have been produced on the basis of a temporally nonuniform set of observations [e.g., *Ohmura et al.*, 1999]. The interest in Greenland ice sheet mass balance is particularly relevant given the dramatic thinning rates observed in the 1990s at low elevations [*Krabill et al.*, 2000]. The thinning is the combined result of ice flow changes and surface ablation. Apparently critical to this thinning is the interplay between water and ice dynamics, providing a mechanism for accelerated ice sheet response to

0148-0227/04/2003JD004451$09.00

climate warming [*Zwally et al.*, 2002]. Data and models both suggest that abrupt climate change during the last glaciation originated through changes in the Atlantic thermohaline circulation in response to small changes in the hydrological cycle [*Clark et al.*, 2002]. The other ice sheet, in Antarctica, is 9 times larger in volume, yet only Greenland exhibits substantial seasonal melting, with runoff representing approximately half the ablation total [*Janssens and Huybrechts*, 2000; *Zwally and Giovinetto*, 2000] and the remainder of ablation coming from surface water vapor fluxes [*Box and Steffen*, 2001; *Déry and Yau*, 2002] as well as iceberg discharge and subglacial melting [*Rignot et al.*, 1997; *Reeh et al.*, 1999]. Surface water vapor mass fluxes are generally small in comparison with precipitation rates; however, the associated latent heat flux represents an important energy sink, without which surface melt rates would be significantly larger.

[3] Global climate models (GCMs) have been used in experiments to simulate ice sheet mass balance under future climate scenarios to relate climate fluctuations to mass balance variability [e.g., *Ohmura et al.*, 1996; *Thompson and Pollard*, 1997; *Glover*, 1999; *Wild and Ohmura*, 2000; *Church et al.*, 2001; *van de Wal et al.*, 2001; *Murphy et al.*, 2002; *Wild et al.*, 2003]. Collectively, the GCM results produce a large envelope of mass balance estimates as a result of the different physical parameterizations used. A major limitation of GCMs is coarse horizontal resolution, currently 100–250 km. At this spatial scale the steep ice sheet margin and ablation zone are not adequately resolved. Further, terrain smoothing along steep ice margins can produce net elevation lowering and results in systematic overestimation of ablation rates from the resulting positive bias in sensible heat flux [e.g., *Glover*, 1999; *Hanna and Valdes*, 2001]. *Wild et al.* [2003] have interpolated GCM temperature fields to a fine (2-km) grid to estimate ablation rates using an empirical model. In a departure from previous results, their projection implies a future dominance of accumulation over ablation in a climate-warming scenario.

[4] Regional climate models (RCMs), operating on horizontal scales of tens of kilometers, offer an attractive alternative to GCMs, automatic weather station networks, and statistical climatologies. RCM applications to the observed past rather than the future benefit from an assimilated set of observations from surface weather stations, atmospheric soundings, and satellite remote sensing, i.e., from atmospheric analyses. As such, RCMs act as physically based interpolators that may be used to address persistent questions in better understanding the magnitude of climate variability over ice sheets, questions nearly impossible to answer, even with much larger surface observational networks. RCMs have the benefit of providing climate data for explicit time periods, as opposed to temporally nonuniform climatologies. Greenland is ideally suited for atmospheric circulation modeling, with prevailing large-scale flow across the domain, unlike Antarctica, where the flow is quasi-concentric; thus less benefit comes from lateral constraints imposed by the atmospheric analyses.

[5] Ice sheet studies with RCMs are increasingly common. *Cassano et al.* [2001] and *Bromwich et al.* [2001a] made a validation study of the Polar Pennsylvania State University–National Center for Atmospheric Research Fifth-Generation Mesoscale Model (Polar MM5) RCM over Greenland using automatic weather station (AWS) data. *Fettweis et al.* [2003] have tested a coupled RCM-snow model using a detailed set of observations from the ETH camp in western Greenland. Using the Modèle Atmosphérique Régional (MAR) RCM, they produce a significantly better treatment of the near-surface state variables than in the relatively coarse European Centre for Medium-Range Weather Forecasts (ECMWF) 15-year reanalysis (ERA-15). *Gallée and Duynkerke* [1997] employed an early version of MAR to investigate modeling surface energy and mass balance over a transect of observational stations for the Greenland Ice Margin Experiment (GIMEX) 1990–1991, citing limited success in simulating basic meteorological variables and surface melting and runoff. *Lefebre et al.* [2003] have validated and applied an evolving albedo model applicable by RCMs. *Box and Rinke* [2003] used the HIRHAM RCM to evaluate multiyear simulations of meteorological and mass balance components over Greenland. The Polar MM5 has been run over the 1991–2000 period to evaluate precipitation in an 8-km nested domain over Iceland (D. H. Bromwich et al., High resolution regional climate simulations over Iceland using Polar MM5: 1991–2000, submitted to *Monthly Weather Review*, 2003). In the present study, we take advantage of 10 years of data availability over Greenland at 24-km horizontal resolution generated in support of the Iceland study.

[6] *Hanna et al.* [2002] and *Mote* [2003] have made significant progress in incorporating RCM, in situ, and remotely sensed data to estimate Greenland ice sheet surface mass balance and runoff. In the latter study, for a 12-year period (1988–1999), there was some evidence that larger runoff is associated with lower accumulation. To derive surface mass balance and runoff, *Mote* [2003] employed a methodology depending on the following: a constant threshold in daily average passive microwave brightness temperature to indicate melting; constant degree day factors for ice or snow melt; precipitation distributed evenly throughout the year; constant spatial distribution of 1995–2000 average sublimation/evaporation rate after *Box and Steffen* [2001]; constant meltwater retention fraction; and liquid precipitation not added to the accumulation rate, but assumed as direct runoff. We pursue a similar methodology, however, with the following differences: calculation of meltwater production based on surface energy balance closure, variable meltwater retention fraction, variable water vapor fluxes from the surface and blowing snow, and liquid precipitation added to melt volume and accumulation.

2. Objectives

[7] The first objective of this study is to reassess the accuracy of the Polar MM5 RCM, under a different model configuration, i.e., from that of *Bromwich et al.* [2001a] and *Cassano et al.* [2001], using in situ observations collected by a network of automatic weather stations (AWS) and supplemented by other glaciological observations. Given this assessment, estimates of surface mass balance components may be produced with better understood uncertainties. Adjusting mesoscale model output based on comparisons with AWS data is explored in an effort to produce more reliable surface mass balance estimates. By analyzing multiple years of RCM output, the variability in surface mass balance components may be gauged. Further, by incorporating interannual surface mass balance results with iceberg

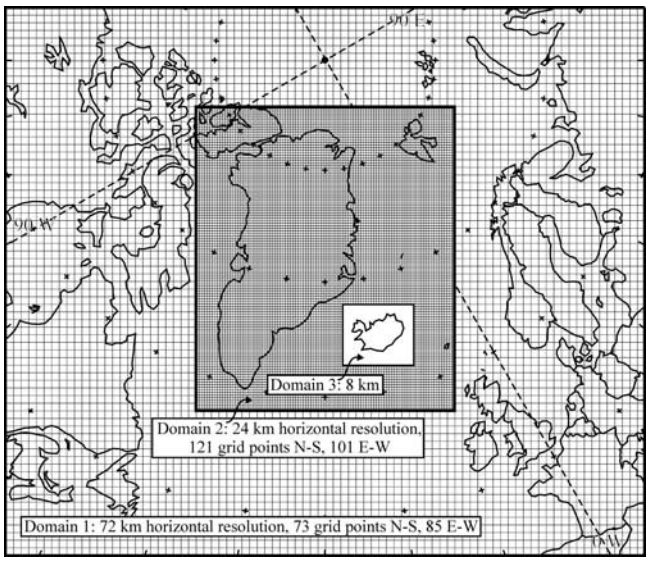

Figure 1. Polar MM5 model domains defined in a 10-year simulation (1991–2000). Data from domain 2 are analyzed in this study. Domain 3, 8-km grid resolution is not shown.

discharge and basal melting estimates, we assess total ice sheet mass balance and provide estimates for the contribution of Greenland ice sheet mass balance to sea level.

[8] Sections 3.1–3.6 describe the atmospheric model, techniques to apply the model data to questions of surface mass balance, the observational data, and methods used for model validation and correction. Maps of the mean surface mass balance components and related meteorological parameters are then presented and discussed in light of previous results and specific regional controls. Integrated total ice sheet surface mass fluxes, equilibrium line variability and sensitivity, and the sensitivity of surface mass balance to temperature and precipitation anomalies are presented in succession. The paper concludes with recommendations about the state of mass balance of the Greenland ice sheet and the challenge of reducing persistent uncertainties.

3. Methods

3.1. Atmospheric Model

[9] The Pennsylvania State University–National Center for Atmospheric Research (NCAR) Fifth-Generation Mesoscale Model (MM5) has been modified for use in polar regions [*Bromwich et al.*, 2001a; *Cassano et al.*, 2001]. The major polar-specific modifications are as follows: explicit ice phase cloud microphysics, polar physical parameterizations for cloud-radiation interactions, stable boundary layer turbulence parameterization, improved treatment of heat transfer through snow and ice surfaces, and implementation of a sea ice surface type.

[10] The model domains configured for this study are shown in Figure 1. Each domain had 28 vertical levels. The lowest two model levels correspond to roughly 14 m and 0 m. The model is run in nonhydrostatic mode with a sixth-order finite-difference scheme after *Chu and Fan* [1997] implemented to improve estimation of vertical motion significant for precipitation formation, particularly along steep slopes.

[11] Polar MM5 was configured to employ a K-theory bulk method for turbulent fluxes (medium-range forecast planetary boundary layer (MRF PBL) scheme), which corrects for missing local gradients in large PBL-scale eddies using a countergradient flux after *Troen and Mahrt* [1986]. The length scales for temperature and humidity were selected to be equal to that for momentum (0.1 mm), although they are probably some fraction of that for momentum [*Garratt*, 1994]. Grid and subgrid precipitation and cloud processes are represented by the same configuration as given by *Bromwich et al.* [2001a]. *Cassano et al.* [2001] includes details for the model options that were selected, including the following: the NCAR Community Climate Model, Version 2 (CCM2), radiation code [*Hack et al.*, 1993] with the Meyers parameterization for ice nuclei concentration; the Reisner mixed-phase cloud parameterization; the two-way nest that allows interaction of atmospheric motion and heat transfer across model domains; and the "multilayer" soil model. The rigid lid upper boundary condition was used. Surface temperature was calculated from the surface energy budget. Sea surface temperature was invariant over each daily simulation. Solar radiation was computed hourly. Model grid cells are represented as homogeneous, i.e., no mixed land/ice points.

[12] The Polar MM5 was initialized at the surface and updated every 12 hours at the lateral boundaries with the 2.5° horizontal resolution ECMWF operational analyses. Although these analyses have the disadvantage of being affected by inhomogeneities due to modifications in the ECMWF assimilation/modeling system over time as well as changes in the global observing system, they were selected because the ERA-15 does not cover when AWS measurements are available and the relatively homogeneous ERA-40 data were unavailable.

[13] The Polar MM5 was run at 24-km horizontal resolution in a series of 30-hour forecasts. The first 6 hours were discarded for model equilibration, and the remaining 24 hours were concatenated into a 6-hourly output time series spanning 1991–2000. With 6-hourly model output it is arguable that the diurnal cycle is inadequately resolved, e.g., for melting. Output data are available for 0600, 1200, 1800, and 2400 UTC (or 0400, 1000, 1600, and 2200 west Greenland standard time). Although solar noon is not represented, data near the warmest and coldest times of day are available. We integrate the 6-hourly data into annual distributions of surface mass balance components, i.e., precipitation P, surface water vapor flux E, blowing-snow sublimation Q_S, and runoff R. The surface mass balance was calculated as P-E-Q_S-R. Model bias versus time into the simulation was investigated, as a short (6-hour) spin-up is suspected to lead to model bias. Earlier simulations used 24-hour spin-up time [i.e., *Cassano et al.*, 2001]. Shorter spin-up time was selected for computational efficiency for this 1.6-times-higher-resolution and 10-times-longer-duration simulation including a high-resolution (8-km) model subdomain (Iceland) not analyzed here. Of note is that the model configuration was not optimized for Greenland; however, this study was pursued given the opportunity to extract useful information from the simulation byproduct over Greenland. The ice sheet area in the 24-km model domain is 1.691×10^6 km^2 and includes 2936 grid cells.

3.2. Surface Energy Balance and Meltwater Production

[14] Changes in surface and subsurface temperatures are directly linked to imbalances in the surface energy budget. In the case of a snow/ice surface, when the melting point has been reached during a period of energy surplus, the excess energy goes into conversion of solid ice into liquid water. As such, meltwater production can be calculated from the residual (Q_M) of the surface energy budget:

$$Q_M = Q_N - (Q_H + Q_E + Q_G + Q_R), \quad (1)$$

where Q_N is the surface net radiative flux. Problematic for melt simulations, the albedo over the ice sheet in this realization of Polar MM5 was fixed at 0.8. To account for this, daily satellite-derived albedos [*Key et al.*, 2002] were applied in surface energy balance calculations of absorbed solar irradiance. Although the temperature-albedo feedback is not considered here, sensitivity studies using Polar MM5 indicate that albedo errors do not greatly affect near-surface air or ice temperatures [*Cassano et al.*, 2001]. Year 2000 albedo values were unavailable; thus monthly climatological values compiled from the 1982–1999 data were used then. Q_H and Q_E are the turbulent sensible and latent heat fluxes, respectively. Q_G is the firn/ice conductive heat flux, incorporating density-dependent effective thermal conductivity after *Sturm et al.* [1997]. A depth-density relationship based on Greenland snow pits is taken from *Box* [2001], and the conductivity estimates are applied only off-line to the model output to estimate Q_G. Although we expect potentially large "soil" temperature errors owing to insufficient spin-up time and biases in climatological soil temperature initialization, we have verified that Q_G represents a small component in the modeled surface energy budget and is of tertiary importance to melting as compared to radiation and turbulent fluxes. Q_R is the sensible heat flux from rain. Q_R may be calculated using the rain T_r and surface temperature T_s

$$Q_R = \rho_w c_w R(T_r - T_s), \quad (2)$$

where ρ_w is the density of water, c_w is the specific heat of water (4.2 kJ kg^{-1} K^{-1}), and R is the rainfall rate (m s^{-1}). T_r is the rain temperature, and T_s is the surface skin temperature. The contribution of Q_R to the ablation rate is assessed here since parts of the ice sheet, particularly in the south, have a maritime character [*Putnins*, 1970]. Volumetric melt M in cubic meters or surface height variation ($dz\ dt^{-1}$) is related directly to Q_M when surface temperature is at or above the melting point, $T_s > 0$°C, as

$$M = Q_M t (L\rho)^{-1}, \quad (3)$$

where t is time (s), ρ is ice density (917 kg m^{-3}), and L is the latent heat of fusion (384 kJ kg^{-1}).

3.3. Blowing-Snow Sublimation

[15] It is important to note that sublimation/evaporation derived from bulk atmospheric profile methods, i.e., that based on Q_E, corresponds to surface water vapor flux only and does not include physics for sublimation from blowing and drifting snow Q_S, now recognized as important in the surface mass budget over snow and ice surfaces [*Pomeroy and Essery*, 1999; *Bintanja*, 2001; *Déry and Yau*, 2002]. In the similar environment over Antarctica, wind-driven sublimation represents one of the major sources of uncertainty in surface mass balance closure [e.g., *Turner et al.*, 2002]. Here, we estimate the blowing-snow sublimation component using a parameterization from *Déry and Yau* [2001], equating Q_S with 10-m wind speed, 2-m air temperature, humidity, and pressure. This parameterization performs similarly to an independent model developed for Antarctica [*Mann et al.*, 2000], compares well with results over a Canadian Arctic land surface, and therefore appears to be applicable over Greenland. The parameterization of *Bintanja* [1998] produced similar results but was not selected owing to uncertainties stated by *Bintanja* [2001].

[16] We evaluate the magnitude of the blowing-snow transport horizontal divergence as *Déry and Yau* [2002] and *Guo et al.* [2003] have done for Antarctica, but we explicitly account for snow availability. Potential blowing-snow transport in the lowest 10 m (Q_{TP}) is estimated using the bulk formulation of *Tabler* [1991] based on Antarctic blowing-snow measurements [*Budd et al.*, 1966]

$$Q_{TP} = {u_{10}^{3.93}}\Big/{290{,}951}, \quad (4)$$

where u_{10} is the 10-m wind speed given by the model and Q_{TP} has units of kg m^{-1} s^{-1} perpendicular to the wind. Snow transport is taken to occur when the wind speed exceeds the temperature-dependent threshold [*Li and Pomeroy*, 1997]. A constant threshold of 7 m s^{-1} was used for temperatures below −27°C owing to unrealistic behavior of the quadratic function in that extreme. Actual snow transport Q_{TA} is estimated using a reduction of Q_{TP} accounting for snow availability A', which is assumed to be unlimited when snow is freshly deposited and decays with time from snow events defined by the model.

$$A' = \left(1.038 + 0.03758t - 0.00014349t^2 + 1.911315e^{-7}t^3\right)^{-1} \quad (5)$$

Time t is in hours after a snowfall event. After 12 days, A' decays to a value of 0.22 that is then held constant and is proportional to the force required to disaggregate bonds of snow particles of that age measured by *Jellinek* [1957]. Q_{TA} is estimated by multiplying values of Q_{TP} by A'. Blowing-snow divergence D is estimated by differencing snow transport at model grid points with the surrounding grid points and represents the combined effect of blowing-snow sublimation and snow redistribution; thus it cannot be used to distinguish blowing-snow sublimation alone.

3.4. Meltwater Retention and Runoff

[17] To gauge runoff, we use the *Pfeffer et al.* [1991] model for meltwater retention, which includes both capillary tension and latent heating effects for a simple uniform wetting front. This method considers meltwater retention for single annual (snow accumulation season) layers only and thus does not consider the case of meltwater percolating into the previous accumulation layer. Consequently, in extremely warm years,

runoff may be overestimated, as annual melt exceeding the accumulation rate is not retained. *Janssens and Huybrechts* [2000] evaluated this and simpler models for meltwater retention using climatological average accumulation and melt. Annual potential meltwater retention fraction p_r, estimated using the annual mean temperature T, snow melt volume M, precipitation P, surface sublimation/evaporation E, blowing-snow sublimation Q_S, specific dry snow accumulation C calculated as P-E-Q_S-liquid precipitation, and the depth of melting d, here is taken as the water equivalent depth of the annual accumulation rate

$$p_r = \left[\frac{c}{L_f} T \frac{d}{P} + \left(\frac{C-M}{P}\right)\left(\frac{\rho_e}{\rho_o} - 1\right)\right], \quad (6)$$

where c is the specific heat of ice (2009 J kg^{-1} K^{-1}), ρ_e is the density of water-saturated snow ($\sim$960 kg m^{-3}), and ρ_o is the average density of dry firn from 0- to 2-m snow depth (353 kg m^{-3}) based on west Greenland snow pits [*Box*, 2001]. In equation (6), M represents the melt of seasonal snow only, i.e., not including glacier ice below the annual accumulation that is found in the net ablation zone. Hence, if melt derived from energy balance closure exceeds the accumulation rate for that year, M is set equal to the accumulation rate in equation (6), allowing the value of p_r to always be positive, and as long as melt calculated by energy balance closure does not exceed the accumulation rate, there is some meltwater retention by percolation and refreeze, i.e., internal accumulation. In cases when M exceeds C, the excess is allowed to run off.

3.5. Interannual Variability

[18] The ability to gauge the absolute and annual variability in ice sheet mass balance components is an attractive capability of regional climate models. Identifying the spatial pattern of year-to-year variability allows identification of regions where largest changes may be taking place. We gauge interannual variability using the 10-year range R of annual values. A 10-year sample is insufficient to define a more robust variability statistic such as the standard deviation σ. The reader is reminded that R increases with the sample size and therefore increasingly exceeds σ with sample size. Variability as defined by R will be more indicative of the absolute variability, not the "standard" variability, i.e., as indicated by $1 \times \sigma$, which represents only 2/3 of the sample variance. Finally, it is important to note that by analyzing the spatial patterns of year-to-year variability, absolute systematic bias effects are minimized.

3.6. In Situ Model Validation Data

3.6.1. Automatic Weather Station Data

[19] In situ observations from Greenland Climate Network (GC-Net) automatic weather stations (AWS) [*Steffen and Box*, 2001] have been of use in evaluating the accuracy of regional climate simulations [e.g., *Cassano et al.*, 2001; *Bromwich et al.*, 2001a; *Hanna and Valdes*, 2001; *Box and Rinke*, 2003]. GC-Net AWS have been installed as part of the NASA Program for Regional Climate Assessment (PARCA) initiative to understand Greenland ice sheet mass balance [*Thomas and PARCA Investigators*, 2001]. Precise station locations are given by *Steffen and Box* [2001]. In this study, GC-Net AWS data from 15 sites (ID numbers 01–15) were compared with 6-hourly Polar MM5 output over a period of relative data abundance (1998–2000). Figure 2 includes the GC-Net AWS distribution and the JAR2 and JAR3 sites 17 and 19. The latter two sites were used only for melt and surface mass balance validation, as they are too close to the ice margin for interpolation using surrounding grid cells. Given that Polar MM5 output represents instantaneous conditions, the comparisons are made with the highest available temporal resolution, i.e., hourly averages. Modeled precipitation is cumulative and therefore does not suffer from lower skill due to the inconsistent sampling between measured and modeled data. We evaluate the model ability to capture both hourly and interannual variability. Root-mean-square (RMS) error was calculated from annual distributions of up to 1464 six-hourly samples.

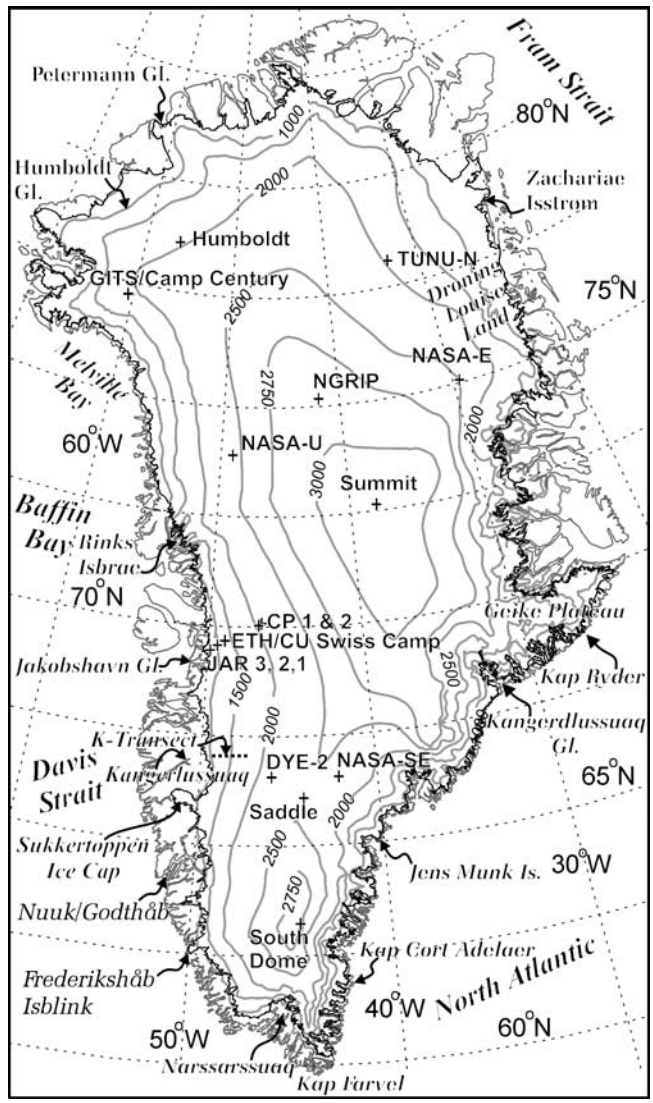

Figure 2. Greenland map featuring inland ice region. Greenland Climate Network (GC-Net) automatic weather station sites are indicated by plus symbols. Locations referred to in the text are included.

[20] Comparisons between gridded 24-km model data and point measurements at the majority of AWS locations are facilitated using bilinear interpolation from the four sur-

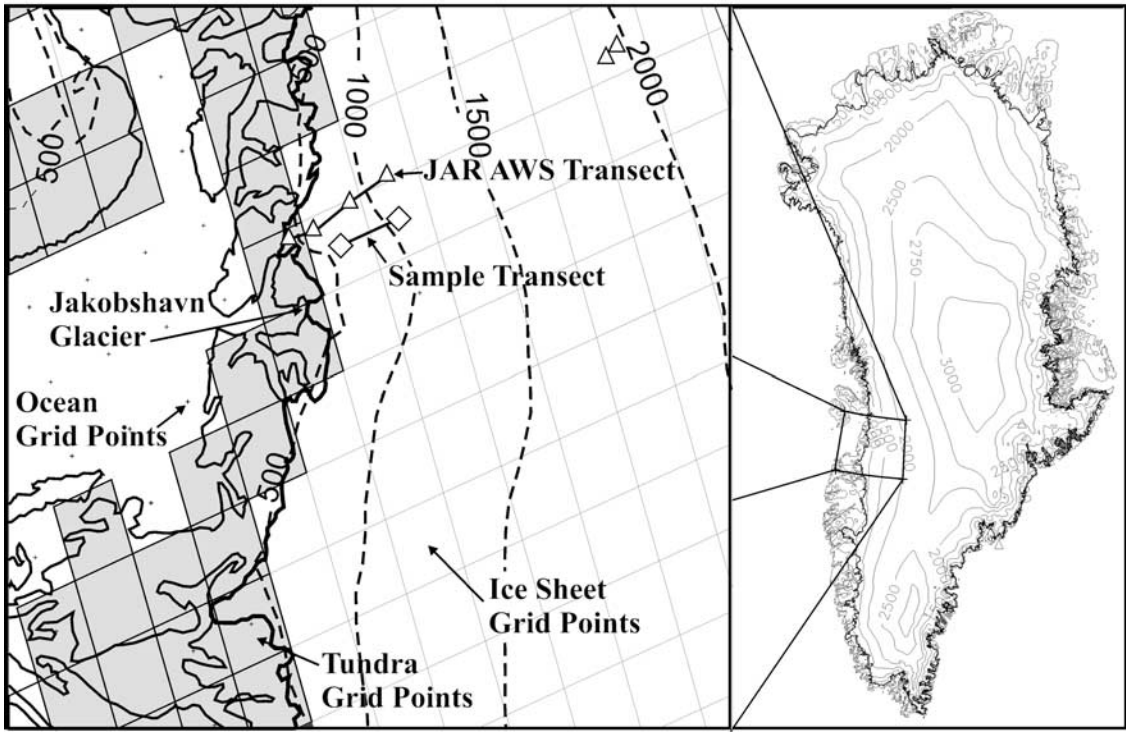

Figure 3. Illustration of model domain over the Jakobshavn Ablation Region (JAR) featuring elevation contour lines and the sample elevation transect used for comparison of model results with AWS locations near the ice sheet margin. Model grid cells with land surface properties corresponding to permanent ice, tundra, and ocean are indicated. Greenland elevation contours are in units of meters above sea level.

rounding model grid values. For AWS sites within 24 km of the ice margin this type of interpolation becomes invalid, given sharply contrasting values resulting from different land surface types in the model, i.e., between ice and tundra or ocean. Also near the ice margin, the spatial gradients are too large to make meaningful comparisons using the closest valid model grid point. To overcome these problems, we have used the nearest similar "sample elevation transect" in the model domain to make comparisons between modeled and observed surface mass balance given a strong elevation dependence. In the Jakobshavn Ablation Region (JAR), three AWS exist below equilibrium line altitude for comparison with Polar MM5 results. The chosen sample transect is nearly parallel and lies 5 km to the south of the AWS transect (Figure 3). Only two grid points were used, i.e., instead of 3 or 4, because the gradient is locally very large and the next model grid point to the west is not over ice.

3.6.2. Surface Mass Balance and Accumulation Rate Data

[21] Ten years of surface mass balance measurements along an elevation transect at 67°N in western Greenland, i.e., the K-transect [*Greuell et al.*, 2001], are useful to evaluate simulated surface mass balance model bias. GC-Net AWS data provide surface mass balance estimates from acoustic height measurements and from snow pit observations made during AWS visits. A small adjustment has been applied to surface height data to account for firn compaction based on compaction measurements from central Greenland [*Hamilton and Whillans*, 2000]. Thus, with surface mass balance data from two independent locations, we may assess, correct, and cross-check modeled values. Ultimately, we compare our surface mass balance results with a parameterization for equilibrium line altitude for the Greenland ice sheet available on the basis of least squares regression of historical glaciological survey data [*Zwally and Giovinetto*, 2001].

3.6.3. Ten-Meter Wind Speed

[22] Over seasonal timescales, GC-Net AWS instruments vary in height above the surface by as much as 3 m owing to accumulation and ablation. Wind speed instruments are placed at two levels on each AWS, separated by 1.2 m. Temperature and wind speed profile data in addition to surface height and pressure measurements are used as inputs into models for the atmospheric surface boundary layer necessary to estimate 10-m wind speeds for comparison with Polar MM5 10-m wind speed. A major uncertainty in the comparison of observed and modeled wind speeds is the effect of buoyant stability on the temperature and wind speed profiles. We rely on boundary layer theory to adjust the observed wind speed profile to estimate 10-m wind speeds from in situ AWS observations, as has been done for AWS data over the Eidgenossische Technische Hochschule/University of Colorado (ETH/CU) Swiss Camp [*Lefebre et al.*, 2003]. A large uncertainty exists in both in situ derived and modeled 10-m wind speed owing to poorly defined stability corrections in the extremely stable surface boundary layer and coarse model resolution near the surface, respectively. However, as the wind speed increases, turbulent mixing minimizes buoyant stability effects, and estimates of 10-m wind speed using in situ profile measurements are likely to be reliable.

Table 1. Annual Summary 6-Hourly Comparison of Polar MM5 Surface Climate Parameters With AWS Data 1998–2000

Parameter	Polar MM5	Mean Bias	Min., Max. Bias[a]	RMSE	Min., Max. RMSE	Mean Correlation r	Min., Max. Correlation r	Number of AWS-Years
2-m air temperature, K	252.3	1.0	−0.01, 2.49	3.6	2.36, 5.36	0.96	0.902, 0.982	41.1
Ground temperature, K	248.3	−2.9	−5.17, −0.87	5.5	3.33, 7.88	0.94	0.839, 0.970	42.2
10-m wind speed, m s^{-1}	8.5	2.6	0.61, 4.57	4.4	3.35, 6.12	0.48	0.232, 0.678	25.6
Sensible heat flux, W m^{-2}	−31.2	−14.1	−36.82, 12.74	32.8	21.64, 46.27	0.37	0.071, 0.654	33.5
Latent heat flux, W m^{-2}	0.3	−16.0	−67.98, −1.85	26.9	8.68, 84.01	0.36	0.011, 0.578	36.6
Outward longwave flux, W m^{-2}	186.2	−40.9	−66.88, −24.53	47.3	33.56, 71.72	0.87	0.724, 0.946	42.2
Downward shortwave flux, W m^{-2}	275.3	8.2	−20.85, 60.93	93.3	53.95, 287.64	0.91	0.377, 0.972	21.0
Albedo, dimensionless	0.85	0.03	−0.03, 0.11	0.10	0.05, 0.19	0.19	−0.093, 0.563	11.0
Specific humidity, g kg^{-1}	1.4	0.0	−0.25, 0.37	0.4	0.28, 0.73	0.92	0.704, 0.960	32.4
Surface pressure, hPa	738.9	2.3	−1.75, 6.71	3.8	1.28, 6.95	0.98	0.899, 0.996	21.1

[a]Min., minimum; Max., maximum.

3.6.4. Two-Meter Air and Surface Temperature and Upward Longwave Radiation

[23] Temperature at a constant height of 2 m is calculated using the observed temperature at two levels, instrument heights, and linear interpolation. Instrument heights are calculated using the initial instrument height upon installation and subsequent surface height change measured by acoustic height sensors. Instrument height error has been checked during site revisits to be within 10 cm. The median heights of GC-Net temperature sensors were 1.4 and 2.6 m, respectively. Surface temperature is estimated using a linear extrapolation of the observed air temperature profile. Only cases when wind speed >4 m s^{-1} are considered to avoid the largest stability and solar overheating errors. Upward longwave radiation has been calculated using the surface temperature estimate and a constant thermal emissivity value of 0.98 and does not include multiple reflection terms.

3.6.5. Shortwave Radiation Data

[24] The GC-Net sites employ a LI-COR 200SZ photoelectric diode to measure incoming and reflected solar radiation in the 400-1100-nm wavelength range. The peak response of this pyranometer occurs at 950 nm. LI-COR reflected shortwave radiation measurements over snow exhibit a positive bias of ~4% that has been corrected on the basis of clear-sky calibrations with Eppley Precision Spectral and Kipp Pyranometer observations. Hourly RMS errors are less than 10%, on the basis of comparisons at Swiss Camp and Summit.

3.6.6. Turbulent Heat Fluxes

[25] Turbulent heat fluxes of sensible Q_H and latent heat Q_E are important components of the surface energy budget over melting snow surfaces [e.g., *Henneken et al.*, 1997]. Q_H and Q_E from Polar MM5 output are available for comparison with that derived from aerodynamic profile calculations applied to the GC-Net AWS data. In situ Q_H calculations follow the procedure given by *Steffen and DeMaria* [1996]. Q_E derived from AWS data is based on *Box and Steffen* [2001] and shows good agreement with eddy correlation and snow lysimeters.

4. Results and Discussion

4.1. Model Comparison With In Situ Observations

4.1.1. Comparison With AWS Data

[26] Model performance over Greenland for basic meteorological variables (pressure, temperature, humidity, wind speed and direction, solar and net radiation) has been assessed using in situ observations independent of the atmospheric analyses in two studies [*Bromwich et al.*, 2001a; *Cassano et al.*, 2001]. The results indicate a high degree of skill in modeled representation of the surface climate over Greenland. Antarctic validation results have been published [*Guo et al.*, 2003] and reveal larger biases owing to weaker constraints from the observational analyses.

[27] In this study, a longer series of surface data and more parameters are compared than in previous Polar MM5 validations. Consistent results were observed from year to year over the 3-year comparison (1998–2000) for all parameters, indicating that potential data homogeneity errors caused by an evolving ECMWF operational analysis product are not of primary importance. Therefore the tabulated results are based on averages over all 15 AWS sites for all 3 years, supplemented with minimum and maximum site-specific annual results to illustrate intersite variability (Table 1). The albedo results in Table 1 are between the AWS observations and the 25-km Extended Advanced Very High Resolution Radiometer (AVHRR) Polar Pathfinder (APP-x) product [*Key et al.*, 2002] for a 2-year comparison, i.e., 1998 and 1999. Model validation statistics listed in this table are for both AWS observed and derived quantities. Derived quantities include turbulent heat fluxes, surface temperature, and outward longwave radiation discussed above.

[28] Through the comparison of up to 42 station years of AWS observations, it became obvious that seemingly small systematic model biases have important consequences to surface energy balance errors. A 2-m air temperature warm bias combined with a cold bias in surface temperature indicates an overly strong surface temperature inversion (STI) in the model. The 2-m air temperature had little or no evolving bias with time into the simulation. However, the surface temperature cold bias increased into the simulation and caused a 40-W m^{-2} (20%) negative bias in upward longwave irradiance (LWU). Not accounting for a 2% reflection of downward longwave irradiance (LWD) in our LWU estimate can account for an LWU error of up to −6 W m^{-2}, which on average would represent an error of less than 10%. The model surface thermal emissivity employs a constant value equal to 0.95. Assuming 0.98 is a correct value [e.g., *Warren*, 1982], ~20% of this negative bias can be explained. We have compared, observed, and modeled LWU and LWD at Summit, on the basis of ventilated Kipp CG4 pyrgeometer data. The results suggested a large underestimate of LWD (−38 W m^{-2}) and have con-

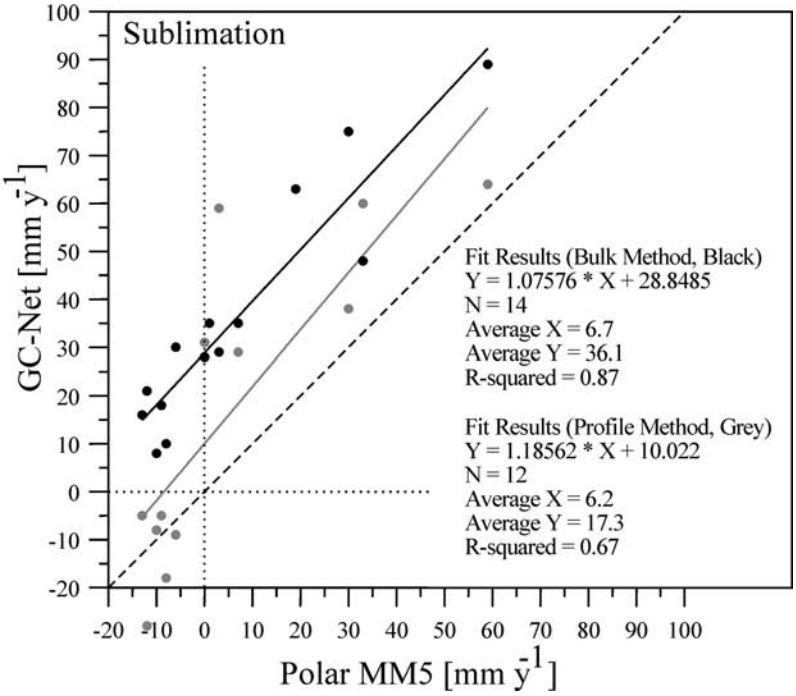

Figure 4. Comparison of annual average model sublimation (1996–1999) with values from 14 GC-Net AWS sites.

firmed the underestimated LWU. A negative LWD bias for clear-sky conditions has also been identified in the CCM2 radiation code [*Pinto et al.*, 1999]. Although the LWU bias contributes to the evolving surface temperature cold bias, we note a cancellation of longwave errors in terms of the net radiation. A 5-W m^{-2} to 10-W m^{-2} (2–5%) positive bias in downward solar irradiance, for Sun angles >10°, contributes to a positive net radiation bias. Modeled 10-m wind speeds exhibit a 2.7 m s^{-1} (32%) positive bias on average, likely due to the overestimated STI, as the wind speed bias also increased on average into each simulation. A 12–15-W m^{-2} (40–50%) average overestimation of the atmosphere to surface sensible heat flux was caused by the overly strong STI, exacerbated by a feedback with overestimated wind speeds. The STI bias leads to a suppression of surface water vapor losses (sublimation), as indicated by a negative bias in surface latent heat flux. Uncorrected, the net surface water vapor mass flux would include a deposition bias. The warm bias in modeled near-surface air temperatures is symptomatic of the persistent inability of atmospheric models to accurately resolve the extreme STI over ice sheets [e.g., *van Lipzig et al.*, 1999; *Box and Rinke*, 2003], implying that either the near-surface vertical resolution and/or stable boundary layer parameterizations are inadequate. A small (−4%) humidity bias was evident from this comparison. Model wind direction errors were consistently within 15° of the observations. Surface pressure variations were extremely well reproduced by the model. AWS sites with accurate elevation measurements, from differential GPS [see *Cassano et al.*, 2001], were used to construct the results for pressure in Table 1, which suggest a 2-hPa positive bias. The negative downward longwave bias persists at 30 hours into the simulation, indicating that this bias is not due to insufficient spin-up time, but suggests insufficient cloud radiative effects. APP-x satellite-derived albedo in comparison with daily AWS observations reveals a small positive bias and RMS error of 0.1. RMS errors reported in Table 1 are based on an annual distribution of 6-hourly samples and are representative of generally larger hourly (not monthly or annual) model error.

[29] Wind speed and humidity biases evident from this comparison are broadly consistent with earlier Polar MM5 comparisons with GC-Net AWS data [*Bromwich et al.*, 2001a; *Cassano et al.*, 2001]. Notable disparities include that *Cassano et al.* [2001] found a cold bias in 2-m air temperature, a negative downward shortwave bias, and a −2-hPa pressure bias. Results in contrast to the previous studies are attributable to less spin-up time in the present configuration and differences in planetary boundary layer model, model resolution, domain size, and domain location. The influence of the latter three differences is not investigated here.

[30] Model skill in representing temporal variability was measured by the Pearson's correlation coefficient r. High model-explained variance r^2 is noted: 96% for surface pressure, 92% for 2-m air temperature, 88% for surface temperature, 85% for humidity, and 83% for downward solar radiation. Less explained variance was evident for wind speed and turbulent heat fluxes. These variables represent an extreme challenge for comparison with mesoscale models owing to highly localized effects in space and time in the observational data. Multiplication of observational errors in turbulent flux calculations further degrades the apparent model skill. Also noteworthy is that parameters that fluctuate around zero or have little trend (e.g., latent heat flux and albedo) typically yield low r values.

4.1.2. Sublimation

[31] Polar MM5 surface water vapor flux values exhibit a systematic negative bias as compared to that derived by bulk (one-level) and profile (two-level) methods [*Box and Steffen*, 2001] applied to AWS data (Figure 4). There are a

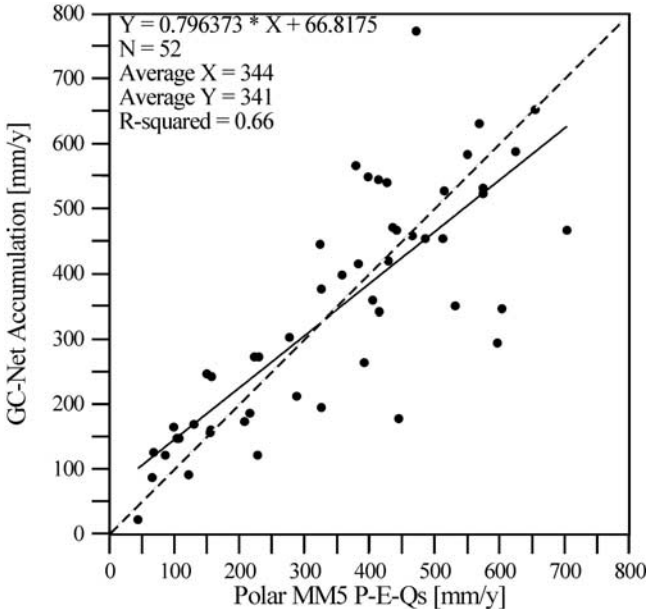

Figure 5. Comparison of annual accumulation rates at AWS sites above equilibrium line altitude (1998–2000) with Polar MM5 results.

different number of data points from one method to the next owing to differing data requirements and availability. There is an offset in Polar MM5 values for the bulk method. When Polar MM5 values are compared with the two-level profile method, there is again a negative bias for positive values (sublimation) but general agreement for negative values (deposition), implying an accurate representation of the water vapor deposition process by the countergradient method of *Troen and Mahrt* [1986]. We conclude that a negative (deposition) bias exists in Polar MM5 simulations, owing to an overly strong surface temperature inversion. We correct this bias in Polar MM5 data on the basis of the "profile" method regression results in Figure 4, since they better represent deposition. This correction produced an average ice sheet total surface water vapor flux in agreement with the climatology of *Box and Steffen* [2001], that of 12% precipitation loss. Without the correction the loss is implied to be 6%.

4.1.3. Blowing-Snow Sublimation

[32] We have applied the parameterization from *Déry and Yau* [2001] to the AWS data and Polar MM5 output. Our comparisons suggest that the positive biases in modeled air temperature and wind speed contribute to a ~60% overestimation of blowing-snow sublimation. Linear regression results of the AWS- and Polar-MM5-derived blowing-snow sublimation (using the same parameterization) have sufficient explained variance ($r^2 = 0.71$) to justify correction of the Polar-MM5-derived blowing-snow sublimation by the inverse of the regression, rather than proceeding with a known bias in blowing-snow sublimation not due to errors in the parameterization.

4.1.4. Precipitation and Accumulation

[33] Polar MM5 simulation of accumulation rate as measured by precipitation minus net surface water vapor flux minus blowing-snow sublimation is compared to accumulation rate derived from snow pit and AWS acoustic height data (Figure 5). The remaining positive bias is suggestive of a residual positive bias in precipitation rate, as we have corrected the bias in net surface water vapor flux and blowing-snow sublimation. In this comparison, however, the distribution of values is not statistically different, as measured by the analysis of variance (ANOVA) statistic. The heteroscedasticity in the scatter may be attributed to many things, including a scale problem when comparing point measurements with 24-km grid cells and the accumulation of both observational and model errors in this multicomponent derivative.

4.1.5. Ablation Zone Surface Mass Balance

[34] Surface height measurements from three AWS in the Jakobshavn Ablation Region (JAR) (Figure 3) were used to assess the accuracy of surface mass balance calculations from Polar MM5. We reconstructed in situ accumulation rates from ablation zone AWS surface height measurements by noting the snow height value at the onset of melt relative to the height of the glacier ice at the end of the previous melt season. Snow water equivalent accumulation has been derived on the basis of snow pit density measurements at these sites. The total water equivalent surface mass balance value was derived given a density assumption for glacier ice with some small air content (i.e., 900 kg m^{-3}). In situ data overlaps with Polar MM5 output are limited to 1996–2000 for JAR1, 1999–2000 for JAR2, and 2000 for JAR3. JAR3 surface mass balance for the year 2000 was estimated using the year 2001 snow accumulation value (0.1-m water equivalence). The average annual surface mass balance estimates from the AWS were −1.4 m, −2.3 m, and −2.8 m, respectively. The Polar MM5 values modeled with the sample transect corresponded to −2.7 m, −3.4 m, and −4.1 m, respectively. Thus the Polar MM5 bias along the JAR transect was −1.3 m, −1.1 m, and −1.3 m, respectively. We attribute this bias to the combined effect of the following: overestimated net radiation and sensible heat flux and the negative bias in latent heat flux caused primarily by too strong surface temperature inversion in this model configuration. For the lowest sites, JAR2 and JAR3, AWS measurements do not indicate the contribution of rain to the surface mass balance, which would somewhat reduce this bias. For the purposes of this comparison we do not try to correct for rain. Rather, we compare Polar MM5 surface mass balance results with the glacier survey results near the K-transect [*Greuell et al.*, 2001] some 280 km to the south. With the K-transect results, we evaluate the Polar MM5 surface mass balance biases for the 1991–2000 average and experimentally adjust the Polar MM5 melt energy magnitude via a simple multiplier of 0.55 to produce a match with the average K-transect equilibrium line altitude over the identical decadal average. The resulting elevation profile of corrected surface mass balance closely resembles the K-transect results, both at equilibrium line altitude (ELA) near 1500 m and the values at the extreme high (1850 m) and low (400-m) elevation limits. We then cross-checked this "global" correction again using the JAR transect surface mass balance observational data. After the K-transect correction the resulting biases correspond to −0.07 m for JAR1, 0.15 m for JAR2, and 0.22 m for JAR3, or within 10% of the surface mass balance magnitude. We proceed using this simple correction to solve the annual surface mass balance for the entire ice sheet.

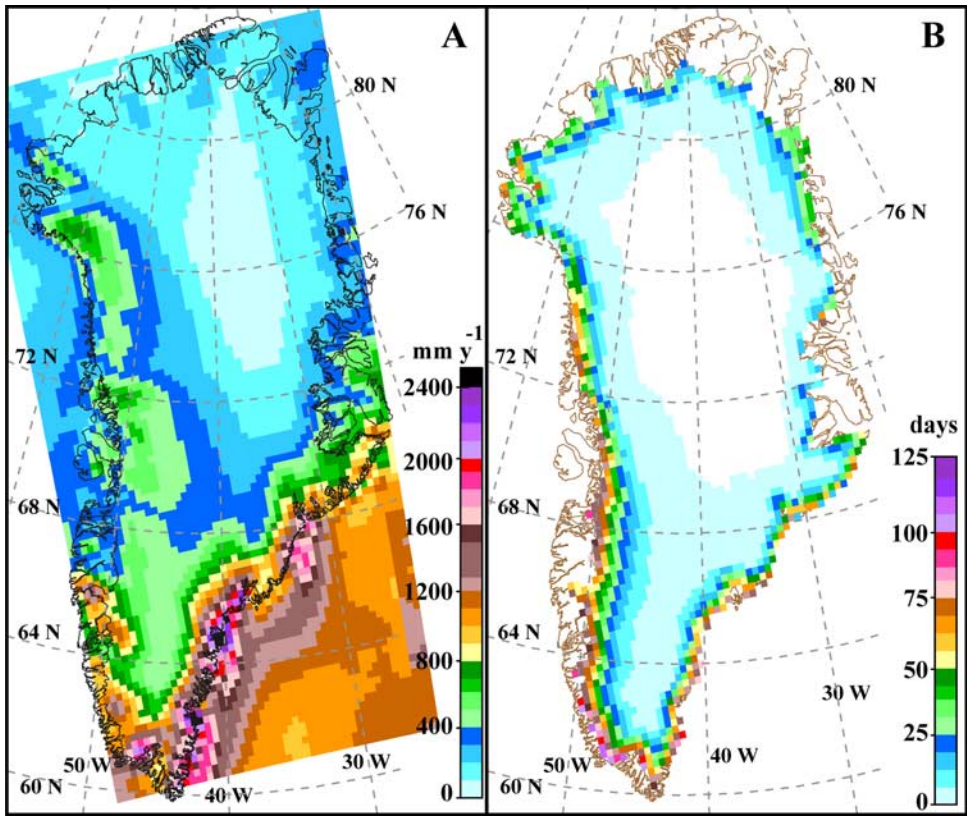

Figure 6. (a) The 1991–2000 average annual total (solid + liquid) precipitation. Non-ice-sheet areas are included for discussion. (b) Annual liquid precipitation percentage of annual precipitation.

4.2. Spatial Distribution of Surface Mass Balance Components

4.2.1. Precipitation

[35] Modeled annual precipitation distributions include widely recognized mesoscale features including maxima found along the southeastern slope, near 72°N along the western slope, and above Melville Bay [e.g., *Ohmura and Reeh*, 1991; *Ohmura et al.*, 1999] (Figure 6a). Regional patterns are also consistent with more recent modeling studies [e.g., *Chen et al.*, 1997; *Bromwich et al.*, 2001b; *Cassano et al.*, 2001; *Hanna et al.*, 2002; *Box and Rinke*, 2003]. Maximum values (>2500 mm yr^{-1}) are simulated over ocean grid cells adjacent to maxima over the ice sheet. Indeed, enhancement of precipitation values is simulated over the seas surrounding much of the ice sheet, indicative of topographic blocking. Greatest differences over the ice sheet among the different estimates are found near the precipitation minimum in the northeast and along the southeast coastal zone. For example, *Cassano et al.* [2001] obtained maximum values exceeding 4000 mm yr^{-1}, probably too large because of imprecision in the calculation of the horizontal pressure gradient force over steep slopes. The maxima found at intermediate elevations around the ice sheet are caused by precipitation enhancement by topographic lifting, i.e., orographic precipitation. Notably, a relative maximum is observed over and to the southeast of the Sukkertoppen Ice Cap, and to the north, there is a precipitation shadow. The model reproduces the regional minimum in precipitation surrounding the airport at Kangerlussuaq, formerly Sondrestrøm Air Force Base and otherwise known as "Greenland's Riviera." In northern Greenland, regional maxima in precipitation are indicative of northerly tracking storms, with greater precipitation rates also concentrated on up-slope paths. Precipitation shadows appear along lee slopes of topographic features, for example, along the western slope of the southern tip of the ice sheet or in the lee of the topographic divide north of Camp Century toward the Humboldt Glacier. Large variability in regional topography of the ice sheet northeast of the Rinks Isbrae is observed in western Greenland at 72°N to coincide with a regional maximum in precipitation. This feature also seems to be linked to the persistent mesoscale low-pressure trough along the west coast.

[36] Extremes values in surface-mass-balance-related parameters over the ice sheet and their geographic coordinates are listed in Table 2. The absolute magnitude of the values and precise locations may still contain biases. Nevertheless, the location (including elevation) of these extremes is of critical interest in glacier climatology and should be more precisely located than is possible even with more dense observational networks.

[37] It is noteworthy that certain parameters, e.g., precipitation, exhibit more than one regional maximum. However, we list only the singular absolute maxima. A maximum in total precipitation and solid precipitation is simulated to occur up glacier from Jens Munk Island in southeast Greenland (Table 2). Minimum precipitation rates of 62 mm yr^{-1} may be underestimated, as compared to results from ice cores, which imply values exceeding 100 mm yr^{-1}, i.e., at Tunu-N [*Mosley-Thompson et al.*, 2001].

Table 2. Ten-Year Average Magnitude and Location of Extremes in Surface-Mass-Balance-Related Parameters Based on Polar MM5 Simulations 1991–2000[a]

Parameter	Value	Latitude, °N	Longitude, °W	Elevation, m
Total precipitation (min.)	63	76.95	39.66	2626
Total precipitation (max.)	2385	64.79	40.67	390
Solid precipitation (min.)	63	76.95	39.66	2626
Solid precipitation (max.)	2224	64.79	40.67	390
Liquid precipitation (min.)	0	–	–	–
Liquid precipitation (max.)	676	61.05	46.12	632
Liquid precipitation fraction (min.), %	0	–	–	–
Liquid precipitation fraction (max.), %	73	61.28	47.67	821
Wind speed (min.), m s^{-1}	3.5	80.47	59.78	98
Wind speed (max.), m s^{-1}	14.9	76.62	24.57	1144
Surface water vapor flux (min.)	−15	68.17	49.89	533
Surface water vapor flux (max.)	674	61.01	44.71	550
Blowing-snow sublimation (min.)	1	70.71	50.52	321
Blowing-snow sublimation (max.)	400	69.35	24.59	552
Snow transport (min.), kg m^{-1} yr^{-1}	3470	66.97	49.99	369
Snow transport (max.), kg m^{-1} yr^{-1}	5,001,564	61.33	43.95	2047
Divergence (min.)	−249	69.16	25.91	1531
Divergence (max.)	345	61.22	44.82	741
Accumulation (min.)	−422	72.51	53.59	637
Accumulation (max.)	1826	64.79	40.67	390
Meltwater production (min.)	0	–	–	–
Meltwater production (max.)	6079	61.79	41.82	413
Runoff (min.)	0	–	–	–
Runoff (max.)	6315	61.79	41.82	413
Surface mass balance (min.)	−6393	61.79	41.82	413
Surface mass balance (max.)	1849	66.06	38.49	1479
2-m air temperature (min.), °C	−30	74.78	35.64	2852
2-m air temperature (max.), °C	−1	65.63	38.33	804
Melt days (min.), days	0	–	–	–
Melt days (max.), days	109	61.28	47.67	821

[a]Surface-mass-balance-related parameters are given in mm yr^{-1}, or are otherwise noted.

[38] According to our simulation, rain constitutes as much as 70% of the annual precipitation rate in coastal regions of southwestern ice sheet (Figure 6b). This fraction can be large in areas where precipitation rates are low, such as near Kangerlussuaq. Values of 10–15% are typical for the southern coastal zone. The contribution of Q_R to the ablation rate is very small for the melting part of the ice sheet as a whole, less than 1% of the total melt energy. We assumed a mixture of liquid and solid precipitation that varied with temperature from 100% liquid precipitation for 2-m air temperatures >4°C to 0% liquid at 0°C. A maximum liquid precipitation value of 676 mm yr^{-1} is simulated over the southern tip of the ice sheet (Table 2).

4.2.2. Surface Water Vapor Flux

[39] The annual sublimation/evaporation maps exhibit the spatial structure that emerges based on spatially interpolated AWS-derived values [*Box and Steffen*, 2001], i.e., an overall water vapor loss for the ice sheet with decreasing loss with increasing elevation, switching to gain on the higher parts of the ice sheet (Figure 7a). This result is consistent with the HIRHAM (using European Center/Hamburg 4 (ECHAM-4) physical parameterizations) model results over Greenland [*Box and Rinke*, 2003]. The 10-year average modeled sublimation/evaporation map includes the region of slight net water vapor deposition of up to +15 mm yr^{-1} centered in the northeast, consistent with AWS-derived sublimation. In the relatively warm year of 1998 the deposition zone was nonexistent, consistent with the correlation of temperature and bulk method surface water vapor flux. A maximum water vapor loss in the northeast near 77°N may be associated with the relatively large wind speeds simulated to occur there. Maximum water vapor mass losses are simulated over the broad ablation zone south of the Jakobshavn glacier (Table 2), where katabatic winds remain strong and humidity is relatively low. Extreme maximum values of surface water vapor loss at southern ice margin grid cells, i.e., >500 mm yr^{-1}, are dominated by evaporation during the six-month melt season in which sublimation is shut off. Not far away, an area of net annual water vapor deposition is simulated along the western slope near the southern tip of the ice sheet near Narssarssuaq (Table 2). Therefore a complex local-scale pattern is evident in the model for this part of Greenland characterized by large orographic variability. Some limited areas of net deposition are also found near the coast in western Greenland, implying a dominance of deposition/condensation in a few special locations, also associated with a complex orographic setting.

4.2.3. Blowing-Snow Sublimation

[40] Blowing-snow sublimation rates, according to the parameterization of *Déry and Yau* [2001], have maximum annual values of 160 mm yr^{-1} and often did not exceed the net surface water vapor flux (Figure 7b). This result is consistent with that of *Déry and Yau* [2002], in which summer surface water vapor flux dominates the annual net water vapor mass balance. Simulated blowing-snow sublimation maxima are found in the southeast, where apparently temperature effects dominate, despite relatively high humidity. Relatively large water vapor mass losses are found in the northeast and west, where the air is less humid and winds are relatively strong.

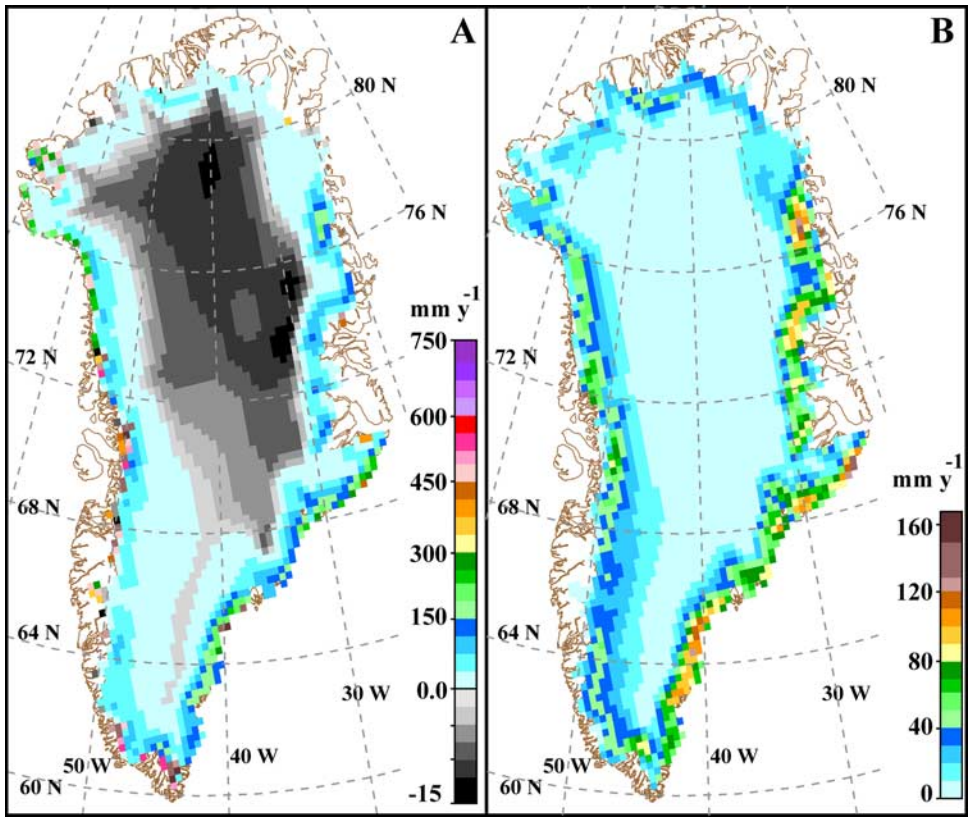

Figure 7. (a) The 1991–2000 average annual net surface water vapor flux. (b) Average annual blowing-snow sublimation rate based on the parameterization of *Déry and Yau* [2001].

4.2.4. Katabatic Winds

[41] The ice sheet has a gently sloping surface over large scales with slope angles generally increasing toward the coast. In the presence of a surface temperature inversion, katabatic winds develop along this sloping surface. The katabatic wind predominates on the annual mean basis owing to the net negative surface radiation balance and dominates the near-surface climate of the ice sheet as evidenced by strong annual wind speeds (4–9 m s^{-1}) and winter wind speed maxima consistent with net radiation variations [*Steffen and Box*, 2001]. Over the ice sheet, near-surface (10-m) wind streamlines are indicative of this close correspondence between wind direction and topography modified by the Coriolis effect (Figure 8a). Simulated wind directions correspond well with AWS observations, including net easterly flow in the vicinity of South Dome, southeasterly flow at North Greenland Ice Core Project (NGRIP), and westerly flow at the Tunu-N AWS. Numerous interesting circulation features are evident, some where AWS do not exist, including channelized flow within glacier topographic basins, e.g., the Kangerdlussuaq glacier. This simulated pattern is similar to the results of *Bromwich et al.* [1996] for wintertime winds, though based on a 10-year average and a much more sophisticated atmospheric model. Streamlines over the adjacent seas are indicative of the persistent low-pressure systems between Iceland and Greenland in the Denmark Strait and in northeast Baffin Bay. These cyclonic patterns explain regional maxima in precipitation in which adjacent coastal regions have net onshore flow. A low-pressure trough along the west Greenland coast manifests in a subsynoptic cyclonic signature in wind streamlines.

[42] The wind speed magnitudes are now described. Curiously, distinct regional annual wind speed maxima (15 m s^{-1}) are simulated to occur over Droning Louise Land and another nunatak region to the south in northeast Greenland (Figure 8a). In the model, these nunatak regions are treated as ice-only owing to inaccurate land surface classification. Thus we speculate the existence of an over-amplified katabatic wind. However, we also note a convergence of wind streamlines. Other than this anomalous region, a strong katabatic wind region (up to 13 m s^{-1}) is simulated at intermediate elevations (~1000–2000 m) surrounding the ice sheet. The summit region also has minimal wind speeds (5 m s^{-1}) owing to less katabatic influence, despite occasionally very strong winds associated with synoptic disturbances. A narrow region along the northern and western ice margin includes the minimum wind speeds for the entire ice sheet. This near-coastal wind lull was not obvious in the earlier relatively coarse (40-km) Polar MM5 simulations [*Cassano et al.*, 2001]. This wind speed reduction has become a well-documented feature for ice sheets, on the basis of AWS observations [e.g., *Wendler et al.*, 1997; *Bintanja*, 1998; *Steffen and Box*, 2001], and has been linked to cold air pooling and a weakening of the katabatic tendency along the ice sheet margin [*Gallée and Pettré*, 1998]. Absolute minimum winds are simulated near the Petermann glacier along the northwestern slope.

4.2.5. Snow Transport and Divergence

[43] Owing to much more abundant snowfall in the southeast as compared to west Greenland, a region of maximum blowing-snow transport and divergence is found over the southeastern slope (Figure 8b). Regions of diver-

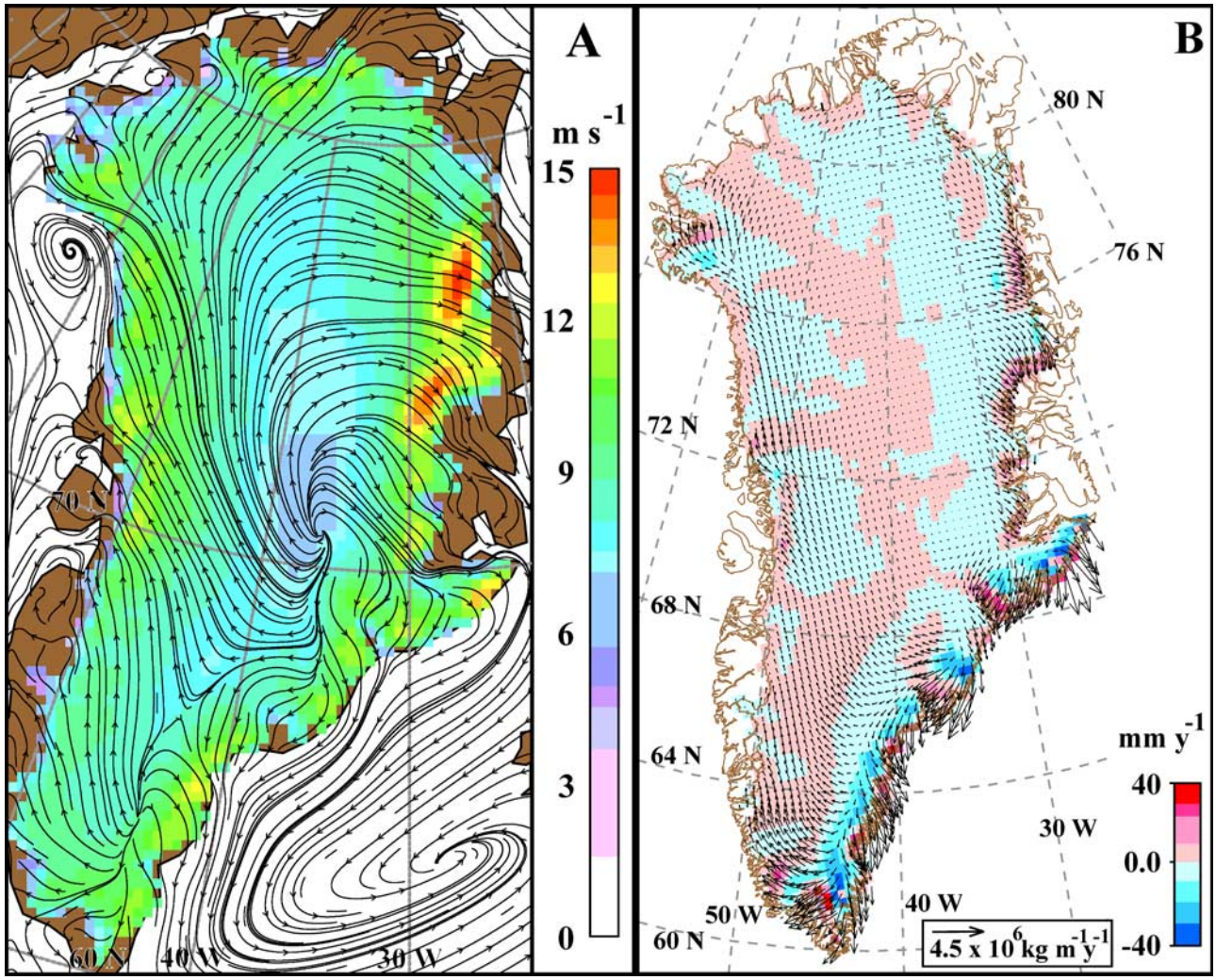

Figure 8. (a) Scalar mean wind speed with vector mean wind direction streamlines for the 1991–2000 period. Ice-free tundra is colored brown. Wind speed magnitudes are shown for the ice sheet only. (b) Blowing-snow transport vectors and spatial divergence patterns.

gence (negative values) are associated with acceleration of the katabatic wind, pronounced along the relatively steep southeastern slope. Convergence zones are evident where katabatic winds decelerate along with blowing-snow transport and in large-scale basins, such as the Kangerdlussuaq glacier, where maximum drift snow convergence of approximately 35 mm yr^{-1} is simulated. Maximum drift snow divergence is simulated in the east over the Geike Plateau north of the Kangerdlussuaq glacier (Table 2). Patterns of drift snow convergence are resolved near the ice margin, owing to decreases in snow transport due to increasing snow entrainment thresholds and deceleration of the katabatic wind. Absolute maximum drift snow convergence is located near Narssarssuaq and near the confluence of the Kangerdlussuaq glacier. The divergence patterns in Figure 8b are a large-scale approximation of the combined effects of spatial changes in snow transport and blowing-snow sublimation. The calculated divergence patterns imply an assumed steady state equilibrium of snow transport and blowing-snow sublimation across the 24-km model grid given that redistribution of individual particles likely cannot exceed even a few kilometers owing to the relatively short ice particle lifetimes in turbulent suspension [e.g., *Schmidt*, 1982]. By assumption of a steady state equilibrium between particle loss by sublimation and the introduction of new particles from saltation impacts, one may infer residual redistribution. However, this may be an invalid assumption for the following reasons: Over the relatively large 24-km length scale, there are nonlinear spatial gradients in wind speed, temperature, and snow availability. Perhaps more importantly, the water vapor flux divergence from the combined effects of spatial divergence of blowing-snow transport and surface snow and blowing-snow sublimation is not explicitly balanced by the parameterizations incorporated here. Therefore we do not attempt to quantify redistribution, i.e., as a residual of the divergence field and Q_S. However, we have attempted experimentally to incorporate the spatial divergence term into the surface mass balance field. The result implied too liberal snow availability in southeast Greenland owing to the fact that precipitation is so often detected there that snow removal can exceed the annual precipitation rate. We must therefore refine the model for snow availability to depend on more than simply time since last snowfall. Elsewhere, the effect of incorpo-

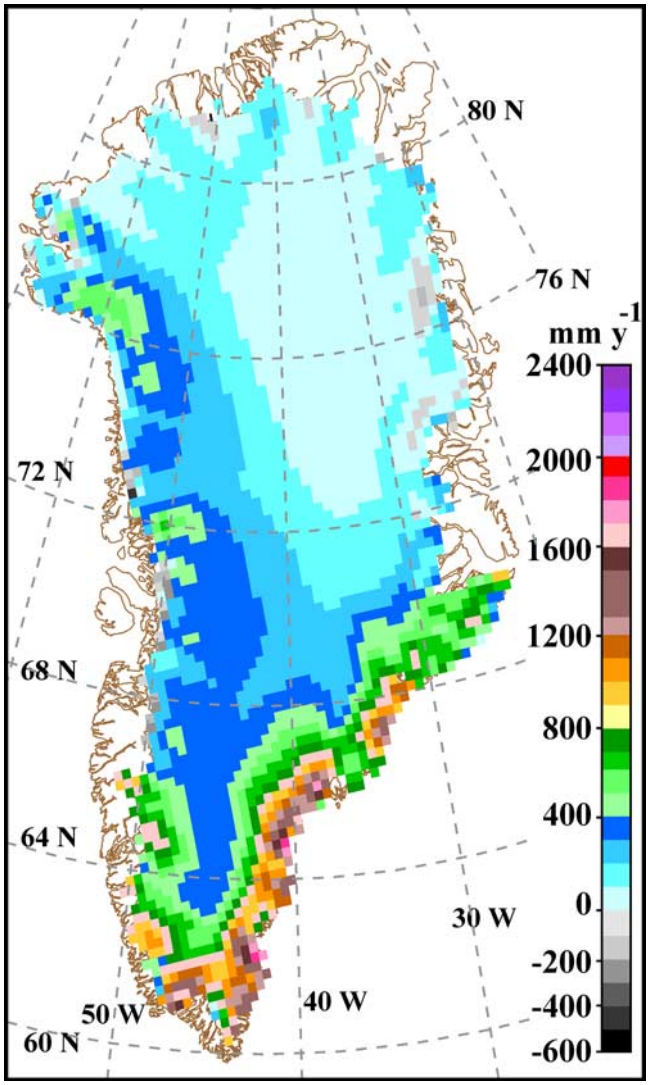

Figure 9. Accumulation 1991–2000, equal to precipitation minus surface snow and blowing-snow sublimation.

rating snow transport divergence had little effect on the surface mass balance distribution. We do not incorporate divergence into our surface mass balance estimates.

4.2.6. Accumulation Rate

[44] The accumulation rate, represented by precipitation minus surface snow and blowing-snow sublimation, is shown in Figure 9 on the same scale as the total precipitation. The spatial distribution closely resembles that of climatologies based on ice cores and snow pits [e.g., *Ohmura et al.*, 1999], again with the dominant orographic maxima cited in the discussion of precipitation results. This presentation of the accumulation distribution contains more detail than in the former climatologies, including regions where net surface water vapor flux apparently exceeds precipitation over Droning Louise Land, resulting in a negative specific accumulation rate, i.e., $A \approx -100$ mm yr^{-1}. Negative accumulation rate implies the presence of blue ice zones, observed from an aerial vantage point and not always in the lee of nunataks. Furthermore, there is evidence of blue ice zones at these locations in NASA Moderate-Resolution Imaging Spectroradiometer (MODIS) satellite observations, but apparently not on such a large scale as implied here. Elsewhere, the accumulation patterns are suggestive of an extremely complex spatial pattern and very large mass fluxes in the southern part of the ice sheet, dominated by precipitation.

4.2.7. Melt

[45] Comparing the total energy for each component of the surface energy balance for the ice sheet as a whole suggests that radiation fluxes provide 99% of the melt energy. This predominance results from the net canceling of turbulent sensible and latent heat fluxes and the fact that the ground heat flux and heat flux from rain collectively represent a very small fraction (less than 0.3%) of the total melt energy.

[46] The spatial distribution of melt days (Figure 10a) indicates maximum melt duration along the southwestern slope, with maximum values near Frederikshåb Isblink. Greater melt frequency in the west versus the east is likely related to less sea ice extent in that region owing to the warm west Greenland current [*Cappelen et al.*, 2001]. Given an apparent 3-K cold bias in surface temperature, the number of melt days must be significantly larger than 109. Maximum meltwater production is simulated near the extreme southeastern slope near Kap Cort Adelaer (Table 2). Other regional melt maxima exist, notably, from Kap Farvel along the southeast slope north to Kap Ryder; along the southwest slope; and in the northeast, near Zachariae Isstrøm.

4.2.8. Runoff

[47] Runoff source regions are concentrated along a narrow strip of the ice sheet near the coast. Concentrated areas of maximum runoff are simulated in the west, on extensive low-lying low-albedo areas, namely, south of the Jakobshavn glacier and on the Frederikshåb Isblink. Spatially discontinuous runoff maxima are evident along the southeast margin and west of Narssarssuaq (Figure 10b and Table 2). Runoff maxima are simulated in southeast Greenland, despite extremely large accumulation rates. Assuming no lateral flow resistance, runoff is simulated to originate as far as 250 km from the coast. The extreme interior values are, however, very small and hardly contribute to the total runoff value.

4.2.9. Surface Mass Balance

[48] The 10-year mean surface mass balance distribution derived by combining simulations of precipitation, surface evaporation/sublimation, blowing-snow sublimation, and runoff is shown in Figure 11a. The spatial structure is indicative of a highly complex pattern in the surface mass balance, with extremely large spatial gradients, e.g., in southeast Greenland, where surface slope and both accumulation and ablation mass fluxes are largest. Regional maxima in positive surface mass balance distinctly emerge in three regions along the western slope, i.e., above the cyclonic feature over northeast Baffin Bay (Figures 6a and 8a), north of Rinks Isbrae at 72°N, and southeast of Nuuk/Godthåb near 63°N. These regional maxima are associated with the topographic enhancement of precipitation rates. The regions of most intense negative surface mass balance occur along the southeast near sea level, and a broad (144 km), more intense melt region exists along the central western slope south of the Jakobshavn glacier. Ablation is

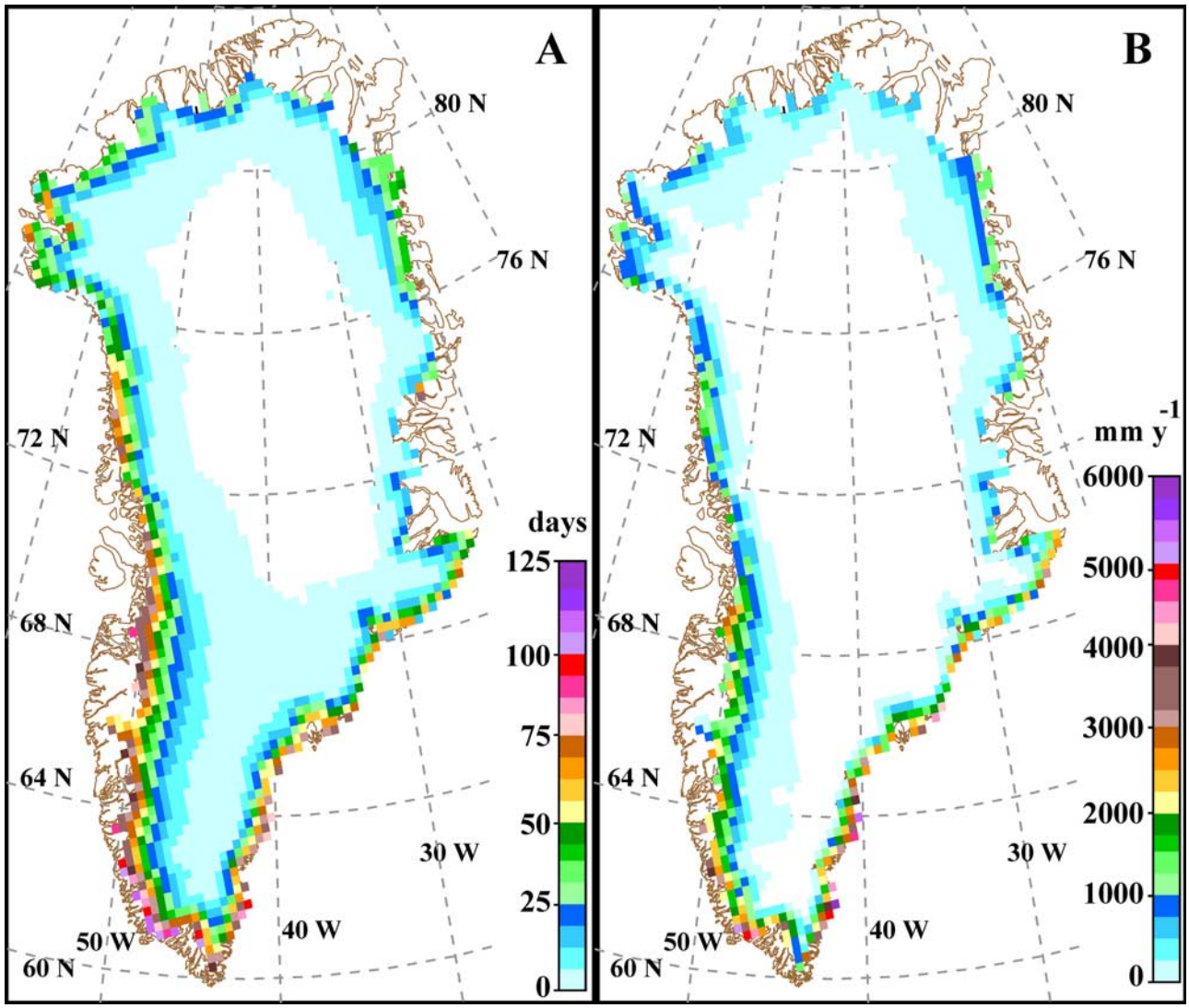

Figure 10. (a) Spatial distribution of melt days, i.e., cases when surface temperatures exceeded the melting point. (b) Average annual total runoff (1991–2000).

simulated to dominate the surface mass balance in broad parts of the north and northeast slope apparently owing to low precipitation rates and low surface slope angles.

[49] We have plotted our result on an equivalent color scale as the independent surface mass balance estimate given by *Zwally and Giovinetto* [2001], hereinafter referred to as ZG2001 (Figure 11b). Both maps exhibit an equivalent macroscale pattern. Largest differences in the spatial structure are notably where there are gaps in the input data for the climatological accumulation distribution used by ZG2001, i.e., along the southeast slope and regarding the precise location of the orographic maximum implied by earlier glacier survey data [i.e., *Ohmura and Reeh*, 1991; *Ohmura et al.*, 1999]. The ZG2001 map does not include as broad of an ablation zone along the northern slope and may be explained by the fact that the ZG2001 result represents an earlier and relatively cold period [*Box*, 2002]. The Polar MM5 result is supported by the observation of 1.4-m net annual surface ablation on the Petermann glacier [*Huff et al.*, 2002]. Another major difference is that the extremes are significantly larger in the Polar MM5 simulations, −6 m to +2 m as compared to −3 m to +1.5 m given by ZG2001, likely because the higher (24-km) Polar MM5 spatial resolution can resolve finer spatial variability compared to the ZG2001 50-km grid.

4.3. Annual Total Ice Sheet Mass Fluxes

[50] Table 3 lists annual total ice sheet mass balance components over the 10-year simulation. Precipitation is the largest single component, which is mostly balanced by surface snow and blowing-snow sublimation, runoff, and iceberg discharge. The magnitude of annual surface snow and blowing-snow water vapor fluxes are nearly equivalent in this simulation, consistent with *Déry and Yau* [2001]. Polar MM5 annual precipitation and water vapor mass fluxes are significantly larger than in the HIRHAM model [*Box and Rinke*, 2003]. Other than the magnitude of these fluxes, the year-to-year variability, as measured by the range in values, is indicative of the background noise, by which a single annual sample could be a poor representative of the normal state of the ice sheet climate. The range of values in integrated mass balance components, such as surface mass

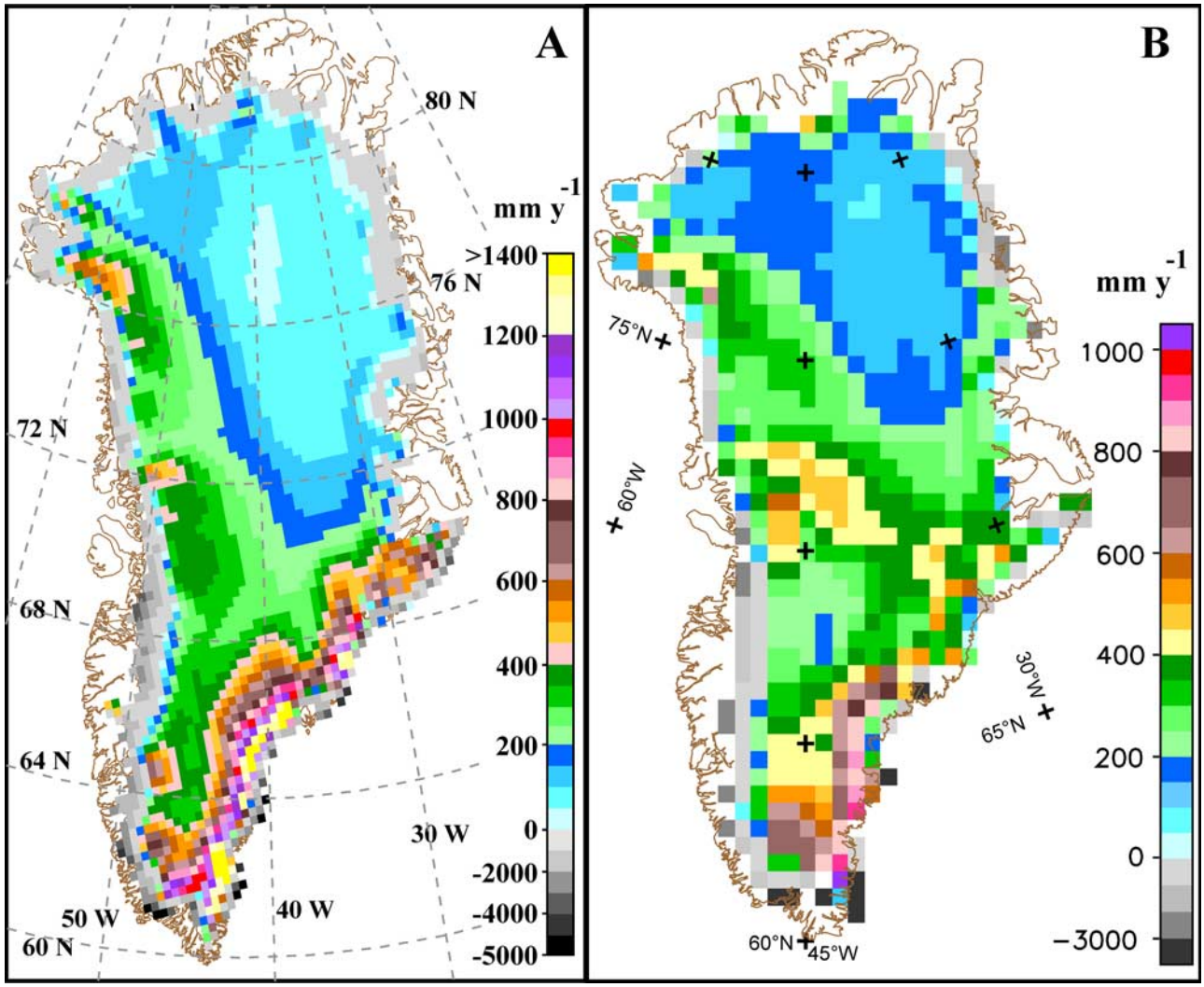

Figure 11. Surface mass balance 1991–2000 (a) based on Polar MM5 simulations and (b) courtesy of *Zwally and Giovinetto* [2001]. Equilibrium line is at the interface of gray and colored grid cells. One minor difference in color tables is that we exchange light yellow with light orange in Figure 11a for values between 400 mm yr^{-1} and 450 mm yr^{-1} to reserve yellows for extremely large surface mass balance in the southeast. The negative scale in Figure 11a spans a larger range than in Figure 11b.

Table 3. Greenland Ice Sheet Mass Balance Components Based on the Polar MM5 Atmospheric Model[a]

Year	Precip.	Surface Sublim./Evap.	Blowing-Snow Sublim.	Melt	Max. Melt Extent[b]	Accum. Area, %	Runoff	p_r,[b] %	SMB[b]	IMB[b]
1992	585	64	41	175	0.96	90.2	127	26.7	353	82
1996	673	58	46	325	0.99	84.9	250	24.6	319	48
1991	629	63	38	402	1.19	82.4	305	23.9	223	−48
2000	624	62	40	401	1.17	82.4	303	22.4	219	−52
1999	595	62	37	370	1.31	83.4	284	22	212	−59
1997	642	67	41	427	1.19	82.9	336	22.4	198	−73
1993	580	56	37	378	1.05	81.0	297	21.9	190	−81
1994	508	60	41	317	1.03	83.5	247	23.7	160	−111
1995	516	63	42	429	1.27	77.9	353	20.7	58	−213
1998	555	71	41	539	1.37	76.6	449	19.3	−6	−277
Mean	591	63	40	376	1.15	82.5	295	22.8	193	−78
Range	165	15	9	364	0.41	13.6	322	7.4	359	359

[a]Components are given in km^3 yr^{-1}. Precip., precipitation, sublim., sublimation; evap., evaporation; accum., accumulation.
[b]Max. melt extent × 10^6 km^2; p_r is the fraction of retained meltwater, SMB refers to surface mass balance, and IMB refers to total ice sheet mass balance.

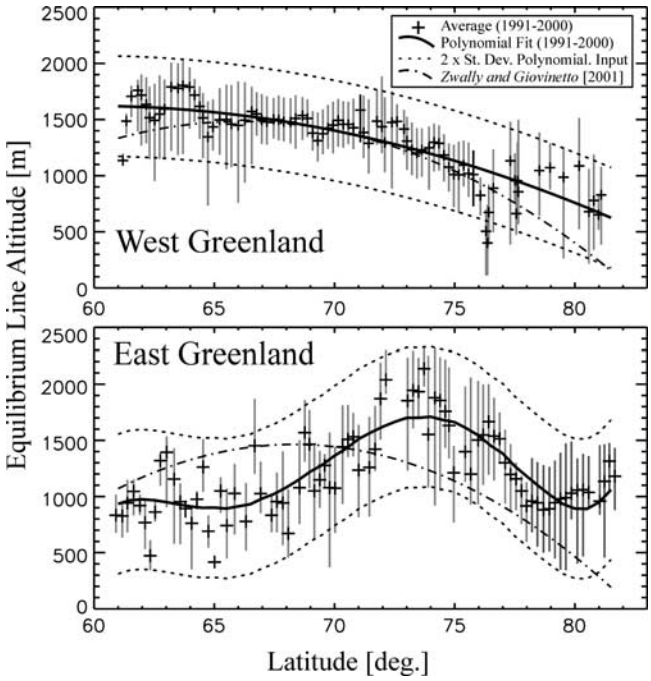

Figure 12. Average, minimum, and maximum equilibrium line altitude variations in Polar MM5 simulations (1991–2000) including parameterizations.

balance and runoff, is as large as the 10-year average magnitude. The effects of an evolving ECMWF operational analysis product will probably contribute to a larger interannual variability in the model results. However, data inhomogeneities are of secondary importance, as determined from Polar MM5 comparisons with AWS data and as temperature and precipitation variability lead to coherent surface mass balance response, as shown in section 4.5. The results in Table 3 are sorted by decreasing surface mass balance. The years 1998 and 1995 stand out as years of relatively small or negative surface mass balance (and maximum runoff) while 1992 and 1996 emerge as maximum positive years with minimum runoff. This pattern is consistent with coastal temperature anomalies and passive-microwave-derived melt extent [*Abdalati and Steffen*, 2001]. Although we find no obvious relationship between accumulation and runoff, as suggested by *Mote* [2003], this hypothesis is consistent with potential retention results; that is, there is less meltwater retention in warm years owing to larger melt relative to accumulation. The average retention fraction p_r for grid cells with less than 100% retention is given and indicates that approximately 23% of accumulated snow is retained as internal accumulation, as compared to 29% used by *Mote* [2003]. Maximum melt extent in our simulations was measured as the count of grid cells where the surface temperature reached the melting point at least in one 6-hourly case. The results from this have proven difficult to compare with measurements of melt extent [e.g., *Abdalati and Steffen*, 2001], given that both techniques employ thresholds and that Polar MM5 can resolve minute amounts of melt that may not be visible in passive microwave data. However, the 30% interannual variations between the two estimates are in agreement.

[51] Using the iceberg discharge (239 $km^3\ yr^{-1}$) and basal melting (32 $km^3\ yr^{-1}$) estimates from *Reeh et al.* [1999], we compute a net negative ice sheet total mass balance for the 1991–2000 decade of $-78\ km^3\ yr^{-1}$. *Zwally and Giovinetto* [2000] derived a value of $-55\ km^3\ yr^{-1}$ representative of a recent climatological value. On the basis of a series of aircraft laser altimeter surveys spanning 1993 to 1999, *Krabill et al.* [2000] derived the total ice sheet balance to be $-46\ km^3\ yr^{-1}$. A more negative mass balance assessment is mainly attributable to the inclusion of mass loss by blowing-snow sublimation and statistically significant (4-K) springtime warming in the 1990s along western Greenland [*Box*, 2002]. The year-to-year range in the surface mass balance is large, $\pm 145\ km^3\ yr^{-1}$. Our mass balance estimate corresponds to a eustatic sea level contribution from Greenland of 2.2 mm (assuming $0.002826\ mm\ km^{-3}$) over the 1991–2000 decade, or approximately 15% of the current estimated $\sim 1.5\ mm\ yr^{-1}$ [*Church et al.*, 2001] sea level rise.

4.4. Equilibrium Line Variations

[52] At elevations where accumulation and ablation balance, i.e., surface mass balance, equals zero, an equilibrium line is said to exist. The general pattern in our simulations is of equilibrium line altitude (ELA) decrease along the western slope of the ice sheet with increasing latitude (Figure 12), consistent with observations summarized by an ELA parameterization available from ZG2001. Polynomial fits to our results are given in Table 4. On a regional scale, inflections in the ELA versus latitude pattern result from regional changes in topography (including precipitation shadow effects) and the proximity of dominant cyclonic systems. The curves also reflect the relative importance of ablation, e.g., a tendency for less melt at lower elevations toward the north. The increase in ELA in west Greenland north of 77°N is caused by the precipitation shadow north of the northwest branch of the ice sheet. In this case, owing to nearly constant regional ablation patterns, ELA increases. The pattern in east Greenland is indicative of a general ELA increase from 60°N to 74°N, followed by a decrease. East Greenland ELA variability exceeds that of west Greenland with 2 standard deviations of the 10-year latitude-varying sample corresponding to 636 m and 447 m, respectively. However, ELA variability varies with latitude and increases

Table 4. Polynomial Coefficients of Parameterized Equilibrium Line Altitude Variations With Latitude Over the East and West Greenland Ice Sheet Slopes

	Coefficient					
	α_0	α_1	α_2	α_3	α_4	α_5
West	−5.9311E + 03	2.5268E + 02	−2.1132E + 00			
East	−3.202998E + 07	2.311199E + 06	−6.648512E + 04	9.530192E + 02	−6.806712	1.937770E-02

in precipitation shadow regions. There is little difference between our results and those of ZG2001 for western Greenland between 65°N and 72°N. Elsewhere in the west, our fit implies either a recent shift in Greenland ice sheet surface mass balance toward increased ablation, an overly negative surface mass balance in our simulation, and/or little constraint of the ZG2001 fit from insufficient observational data. To corroborate an increased ablation rate, the ZG2001 ELA parameterization reflects observations from a generally earlier time period (1960s to 1990s) characterized by cooling [*Box*, 2002]. In east Greenland, little agreement between our results and those of ZG2001 is evident. Our simulations indicate a much more complex east Greenland ELA pattern. Important to note is that apparently nowhere over the ice sheet is ELA at or below sea level.

4.5. Surface Mass Balance Sensitivity

[53] Simulated temperature and precipitation anomalies for annual melt seasons (1 April to 30 September) exhibit meaningful correlations with simulated surface mass balance anomalies. Interannual accumulation and ablation variability causes equilibrium line altitude (ELA) fluctuations. Therefore ELA provides a useful indicator of the combined influence of thermal and precipitation forcing on surface mass balance. West Greenland ELA thermal variability is characterized by average sensitivity of +98 ± 40 m K^{-1}, while east Greenland sensitivity is +109 ± 68 m K^{-1}, larger apparently from larger surface slope. *Ambach* [1989] estimated perturbations in ELA under different climate scenarios, including a general 79-m positive shift in ELA given a 1-K warming and 10% precipitation rate increase with a negligible influence of cloud amount anomalies. The results of our simulations indicate that the sensitivity of ELA to temperature and precipitation anomalies, however, varies significantly with latitude, dominated by regional accumulation and to a lesser extent ablation variability. ELA sensitivity to precipitation generally decreases with latitude from −200 m (mm yr^{-1})$^{-1}$ at 61°N to −1500 m (mm yr^{-1})$^{-1}$ at 72°N along the west and east slopes. This trend is interrupted along the eastern slope by the complex of mountains, while along the western slope, the ELA sensitivity decreases to roughly 60 m (mm yr^{-1})$^{-1}$ at 70°N followed by an increase to the northern limit approaching an extreme in sensitivity of 2500 m (mm yr^{-1})$^{-1}$. The general pattern of ELA sensitivity to temperature and precipitation anomalies suggests a dominance of thermal factors on surface mass balance in the southern part of Greenland, with a relative increase in the importance of precipitation anomalies as the thermal sensitivity decreases with increasing latitude.

[54] *Zuo and Oerlemans* [1997] deduced values of surface mass balance sensitivity ranging from −30 to −97 mm yr^{-1} K^{-1} for specific regions over the Greenland ice sheet using an empirical model for summer temperature anomalies based on terrestrial station data. In the following, we evaluate surface mass balance sensitivities based on annual and seasonal anomalies. First, we found no correlation of annual mean temperature anomalies with surface mass balance anomalies for the entire elevation range of the ice sheet. If only the area below ELA defined using the polynomials in Table 4 is considered, a sensitivity of −90 mm yr^{-1} K^{-1} (r = −0.50) to annual temperature variability is evident. When considering only the summer (JJA) temperature anomalies, the sensitivity for the whole ice sheet is −13 mm yr^{-1} K^{-1} (r = −0.82), and for the area below ELA the sensitivity is −64 mm yr^{-1} K^{-1} (r = −0.95), keeping in mind, however, that some runoff originates from above ELA. It is noteworthy that both 1992 occupies the largest positive surface mass balance anomaly and the most negative temperature anomaly and 1998 exhibits the opposite pattern. The years 1991, 1996, and 2000 defy this pattern and suggest other dominant factors, namely, precipitation. Therefore a more meaningful sensitivity is based on the multiple regression of surface mass balance anomalies with temperature and precipitation anomalies. The regression equation for surface mass balance dependence (mm yr^{-1}) on annual anomalies for the entire ice sheet is

$$\Delta\mathrm{SMB} = -49.5\Delta T + 1.41\Delta P, \tag{7}$$

where ΔT is the annual temperature anomaly in K yr^{-1} and ΔP is the annual precipitation anomaly in mm yr^{-1} (r = 0.87). When the temperature variability from summer only is considered, with annual precipitation, the result is

$$\Delta\mathrm{SMB} = -12.3\Delta T + 0.67\Delta P \tag{8}$$

and is characterized by a high correlation (r = 0.96) and smaller sensitivities because seasonal temperature anomalies are relatively large. If only the area below ELA and summer anomalies are considered, the correlation coefficient remains high (r = 0.96), and the sensitivity is

$$\Delta\mathrm{SMB} = -65.1\Delta T + 0.33\Delta P. \tag{9}$$

However, equation (9) is heavily biased in terms of ΔP by 1992, which is in contrast to the general pattern, with both the largest negative precipitation anomaly and the largest positive surface mass balance anomaly. The year 1992, therefore, defies a typical climate sensitivity and has been linked with cooling associated with the Mount Pinatubo volcanic eruption [*Abdalati and Steffen*, 1997]. For general climate sensitivity simulations we recommend equation (8).

[55] *Wild et al.* [2003] project that in a future climate-warming scenario, precipitation rates over Greenland may increase and even dominate surface mass balance change. With our limited 10-year sample, we find a small yet statistically insignificant positive correlation (r = 0.31) between annual temperature and precipitation anomalies. In the extreme warmest (1998) and coldest (1992) years of our sample, for example, there is no apparent correlation between temperature and precipitation anomalies, despite a robust correlation with surface mass balance. Therefore it seems that thermal factors dominate Greenland surface mass balance sensitivity rather than precipitation variations.

5. Conclusions

[56] The Polar MM5 regional climate model, run over Greenland for 10 years (1991–2000), has provided new insight into spatial and temporal patterns of ice sheet surface mass balance variability. Unprecedented spatial details of glaciometeorological patterns over the Greenland ice sheet have been resolved with the relatively high 24-km model horizontal resolution, as compared with previous global climate model (GCM) studies. A major advantage of a

regional climate model approach over statistical climatologies is to evaluate interannual variability, which indicates meaningful links between temperature and precipitation anomalies and surface mass balance.

[57] We have evaluated the relative importance of numerous terms in the surface mass balance and conclude that melting is a dominant process in Greenland surface ice sheet mass balance, as compared to precipitation. The range in mass balance parameters over the 10 annual simulations (1991–2000) is suggestive of extremely large year-to-year variability. For example, the 10-year range in ice sheet surface mass balance values is equivalent to the magnitude of this flux. However, some of this variability may be attributable to changes in the archived ECMWF operational analyses over the 10-year period. Runoff variability, simulated given meltwater production estimates and a simple annual meltwater retention model, is characterized by 50% interannual variability. Other parameters exhibit large interannual variability. However, it is this variability that is of primary interest in understanding ice sheet response to climate changes. Using an estimate for iceberg discharge, we conclude that Greenland ice sheet mass balance, as a whole, is negative and has contributed ~1.5 mm to eustatic sea level change over the 1991–2000 decade. In comparison with earlier estimates, Greenland ice sheet mass balance appears to have become more negative, consistent with coastal temperature increases observed during this decade. The general pattern of equilibrium line altitude sensitivity to temperature and precipitation anomalies suggests a dominance of thermal factors on surface mass balance in the southern part of Greenland, with a relative increase in the importance of precipitation anomalies as the thermal sensitivity decreases with increasing latitude.

[58] A number of meaningful conclusions about specific processes relevant to ice sheet mass balance are now made. Because of the general net canceling of turbulent sensible and latent heat fluxes in the windy part of the ablation zone, the predominant source of melt energy is net radiation. Although liquid precipitation appears to contribute as much as 70% of the annual total precipitation for near-coastal glaciers in the extreme maritime south, the direct contribution of rain to melt rates over the ablation zone as a whole appears to be extremely small. Although albedo reductions owing to rain on snow events are certainly influential for melt onset, these were not investigated here. Regional maxima and minima in precipitation are linked with topographic variations in the context of dominant storm tracks. The surface net water vapor flux distribution includes the region of net water vapor deposition of up to +15 mm yr^{-1} and covering much of the area above ~2700-m elevation, a result consistent with net surface water vapor flux derived from automatic weather station observations. However, also including blowing-snow sublimation may render the net surface water vapor flux negative over the entire ice sheet. A regional maximum in precipitation in western Greenland at 72°N coincides with relatively high variability in regional topography. Finally, minimum snow accumulation is negative given an apparent dominance of ablation, particularly in the form of modeled blowing-snow sublimation, at a location where precipitation rates are low and simulated strong winds contribute to large water vapor losses.

[59] In situ observations from automatic weather station (AWS) networks supplemented by glaciological surveys are critical for assessing atmospheric model accuracy and for gaining insight into the causes of model biases. On the basis of model comparisons with AWS data, it became clear that temporal variability was well captured by the model; however, systematic (absolute) model biases, some seemingly small, were shown to have important consequences for surface energy balance, particularly when energy balance closure is exploited to derive meltwater volume. Model results depend strongly on model configuration, including spin-up time and land surface modeling (including surface albedo and meltwater retention). We conclude that each model configuration requires some accuracy assessment, even for seemingly small configuration changes, e.g., spatial resolution. This assessment is required not only for the state variables, i.e., temperature, humidity, pressure, and wind speed, but also for derivatives of the state variables, i.e., turbulent energy fluxes. Further, glaciohydrologic data from snow pits, ice cores, and ablation stakes are vital to assess modeled surface mass fluxes, i.e., accumulation rates and meltwater runoff. Given a sufficiently large sample of in situ observations from AWS networks and glaciological surveys, it was possible to construct statistical corrections to modeled melt energy biases to produce more realistic estimates for surface mass balance components including melt energy and blowing-snow sublimation rate. Comparisons with in situ observations thus have provided the basis for clear recommendations for future model development. These include an emphasis on a more detailed land surface (firn) model with more appropriate spin-up time to allow attainment of full cloud and precipitation development. With such refinements, regional climate model simulations will become an important bridge between AWS networks and large-scale climate studies based on remote-sensing techniques for the purpose of better understanding the ice sheet response to climate change.

[60] Given the large uncertainties in the several mass balance components involved, our estimates lack an absolute uncertainty estimate. Further, the natural variability in ice sheet mass balance appears to be too large to provide an indisputable assessment of positive or negative mass balance. However, it is clear that warming would produce a negative mass balance trend. Future work must attempt to construct uncertainty estimates. This is a challenging task, given that there are currently insufficient observational data to firmly constrain ice sheet mass balance as a whole. Future work should be concerned with developing a model configuration that does not require empirical adjustment.

[61] **Acknowledgments.** This work was supported by NASA grants NAG5-12407 and NAG5-11749 and the Byrd Postdoctoral Fellowship program. S. J. Déry has provided code and a test data set to verify the proper functioning of the blowing-snow sublimation parameterization. Comments from M. R. van den Broeke, J. Cassano, and one anonymous reviewer were extremely valuable. We thank K. Steffen for the Summit radiation data, H. J. Zwally for the use of his color table, and M. Giovinetto and H. J. Zwally for the mass balance figure. N. Cullen assisted with AWS maintenance and in obtaining snow pit data. This is contribution 1296 of the Byrd Polar Research Center.

References

Abdalati, W., and K. Steffen (1997), Snowmelt on the Greenland ice sheet as derived from passive microwave satellite data, *J. Clim.*, *10*, 165–175.

Abdalati, W., and K. Steffen (2001), Greenland ice sheet melt extent: 1979–1999, *J. Geophys. Res.*, *106*(D24), 33,983–33,988.

Ambach, W. (1989), Effects of climatic perturbations on the surface-ablation regime of the Greenland ice sheet, west Greenland, *J. Glaciol.*, *35*(121), 311–316.

Bintanja, R. (1998), The contribution of snowdrift sublimation to the surface mass balance of Antarctica, *Ann. Glaciol.*, *27*, 251–259.

Bintanja, R. (2001), Snowdrift sublimation in a katabatic wind region of the Antarctic ice sheet, *J. Appl. Meteorol.*, *40*, 1952–1966.

Box, J. E. (2001), Surface water vapor exchanges on the Greenland ice sheet derived from automated weather station data, Ph.D. thesis, Univ. of Colo., Boulder.

Box, J. E. (2002), Survey of Greenland instrumental temperature records: 1873–2001, *Int. J. Climatol.*, *22*, 1829–1847.

Box, J. E., and A. Rinke (2003), Evaluation of Greenland ice sheet surface climate in the HIRHAM regional climate model, *J. Clim.*, *16*, 1302–1319.

Box, J. E., and K. Steffen (2001), Sublimation estimates for the Greenland ice sheet using automated weather station observations, *J. Geophys. Res.*, *106*(D24), 33,965–33,982.

Bromwich, D. H., Y. Du, and K. M. Hines (1996), Wintertime surface winds over the Greenland ice sheet, *Mon. Weather Rev.*, *124*, 1941–1947.

Bromwich, D. H., J. Cassano, T. Klein, G. Heinemann, K. Hines, K. Steffen, and J. E. Box (2001a), Mesoscale modeling of katabatic winds over Greenland with the Polar MM5, *Mon. Weather Rev.*, *129*, 2290–2309.

Bromwich, D. H., Q. S. Chen, L. S. Bai, E. N. Cassano, and Y. Li (2001b), Modeled precipitation variability over the Greenland ice sheet, *J. Geophys. Res.*, *106*(D24), 33,891–33,908.

Budd, W. F., W. R. J. Dingle, and U. Radok (1966), The Byrd Snow Drift Project: Outline and basic results, in *Studies in Antarctic Meteorology*, *Antarct. Res. Ser.*, vol. 9, pp. 71–134, AGU, Washington, D. C.

Cappelen, J., B. V. Jørgensen, E. V. Laursen, L. S. Stannius, and R. S. Thomsen (2001), The observed climate of Greenland, 1958–99: With climatological standard normals, 1961–90, *Tech. Rep. 00–18*, 152 pp., Dan. Meteorol. Inst., Copenhagen.

Cassano, J., J. E. Box, D. H. Bromwich, L. Li, and K. Steffen (2001), Verification of Polar MM5 simulations of Greenland's atmospheric circulation, *J. Geophys. Res.*, *106*(D24), 33,867–33,890.

Chen, Q.-S., D. H. Bromwich, and L.-S. Bai (1997), Precipitation over Greenland retrieved from a dynamic method and its relation to cyclone activity, *J. Clim.*, *10*, 839–870.

Chu, P. C., and C. Fan (1997), Sixth-order difference scheme for sigma coordinate ocean models, *J. Phys. Oceanogr.*, *27*, 2064–2071.

Church, J. A., J. M. Gregory, P. Huybrechts, M. Kuhn, C. Lambeck, M. T. Nhuan, D. Qin, and P. L. Woodworth (2001), Changes in sea level, in *Climate Change 2001: The Scientific Basis*, edited by J. T. Houghton et al., pp. 639–694, Cambridge Univ. Press, New York.

Clark, P. U., N. G. Pisias, T. F. Stocker, and A. J. Weaver (2002), The role of the thermohaline circulation in abrupt climate change, *Nature*, *415*, 863–869, doi:10.1038/415863a.

Cuffey, K. M., and S. J. Marshall (2000), Substantial contribution to sea-level rise during the last interglacial from the Greenland ice sheet, *Nature*, *404*, 591–594.

Déry, S. J., and M. K. Yau (2001), Simulation of blowing snow in the Canadian Arctic using a double-moment model, *Boundary Layer Meteorol.*, *99*(2), 297–316.

Déry, S. J., and M. K. Yau (2002), Large-scale mass balance effects of blowing-snow and surface sublimation, *J. Geophys. Res.*, *107*(D23), 4679, doi:10.1029/2001JD001251.

Fettweis, X., J. P. van Ypersele, H. Gallée, and F. Lefebre (2003), Modelling of the 1991 Greenland summer with the coupled atmosphere-snow regional climate model MAR, paper presented at 7th International Conference on Polar Meteorology and Oceanography, Am. Meteorol. Soc., Hyannis, Mass., 12–16 May.

Gallée, H., and P. G. Duynkerke (1997), Air-snow interactions and the surface energy and mass balance over the melting zone of west Greenland during the Greenland Ice Margin Experiment, *J. Geophys. Res.*, *102*(D12), 13,813–13,824.

Gallée, H., and P. Pettré (1998), Dynamical constraints on katabatic wind cessation in Adélie Land, Antarctica, *J. Atmos. Sci.*, *55*, 1755–1770.

Garratt, J. R. (1994), *The Atmospheric Boundary Layer*, 334 pp., Cambridge Univ. Press, New York.

Glover, R. (1999), Influence of spatial resolution and treatment of orography on GCM estimates of the surface mass balance of the Greenland ice sheet, *J. Clim.*, *12*, 551–563.

Greuell, W., B. Denby, R. S. W. van de Wal, and J. Oerlemans (2001), Ten years of mass-balance measurements along a transect near Kangerlussuaq, Greenland, *J. Glaciol.*, *47*(156), 157–158.

Guo, Z., D. H. Bromwich, and J. J. Cassano (2003), Evaluation of Polar MM5 simulations of Antarctic atmospheric circulation, *Mon. Weather Rev.*, *131*, 384–411.

Hack, J. J., B. A. Boville, B. P. Briegleb, J. T. Kiehl, P. J. Rasch, and D. L. Williamson (1993), Description of the NCAR Community Climate Model (CCM2), *NCAR Tech. Note NCAR/TN-382 + STR*, 108 pp., Natl. Cent. for Atmos. Res., Boulder, Colo.

Hamilton, G. S., and I. M. Whillans (2000), Point measurements of the mass balance of the Greenland ice sheet using precision vertical GPS surveys, *J. Geophys. Res.*, *105*(B7), 16,295–16,301.

Hanna, E., and P. Valdes (2001), Validation of ECMWF (re)analysis surface climate data, 1979–1998, for Greenland and implications for mass balance modelling of the ice sheet, *Int. J. Climatol.*, *21*, 171–195.

Hanna, E., P. Huybrechts, and T. Mote (2002), Surface mass balance of the Greenland ice sheet from climate analysis data and accumulation/runoff models, *Ann. Glaciol.*, *35*, 67–72.

Henneken, E. A. C., A. G. C. A. Meesters, N. J. Bink, H. F. Vugts, and F. Cannemeijer (1997), Ablation near the equilibrium line on the Greenland ice sheet, southwest Greenland, July 1991, *Z. Gletscherkd. Glazialgeol.*, *33*(2), 173–184.

Huff, R., N. J. Cullen, and K. Steffen (2002), AWS measurements of surface ablation on the Petermann Gletscher, Greenland, *Eos Trans. AGU*, *83*(47), Fall Meet. Suppl., F314.

Janssens, I., and P. Huybrechts (2000), The treatment of meltwater retention in mass-balance parameterizations of the Greenland ice sheet, *Ann. Glaciol.*, *31*, 133–140.

Jellinek, H. H. G. (1957), Compressive strength properties of snow, 16 pp., U.S. Army Snow Ice and Permafrost Estab., Hanover, N. H.

Key, J., C. Fowler, J. Maslanik, T. Haran, T. Scambos, and W. Emery (2002), The Extended AVHRR Polar Pathfinder (APP-x) Product, v 1.0, digital media, Space Sci. and Eng. Cent., Univ. of Wisc., Madison.

Krabill, W., W. Abdalati, E. Frederick, S. Manizade, C. Martin, J. Sonntag, R. Swift, R. Thomas, W. Wright, and J. Yungel (2000), Greenland ice sheet: High-elevation balance and peripheral thinning, *Science*, *289*, 428–430.

Lefebre, F., H. Gallée, J.-P. van Ypersele, and W. Greuell (2003), Modeling of snow and ice melt at ETH Camp (west Greenland): A study of surface albedo, *J. Geophys. Res.*, *108*(D8), 4231, doi:10.1029/2001JD001160.

Li, L., and J. W. Pomeroy (1997), Estimates of threshold wind speeds for snow transport using meteorological data, *J. Appl. Meteorol.*, *36*, 205–213.

Mann, G. W., P. S. Anderson, and S. D. Mobbs (2000), Profile measurements of blowing-snow at Halley, Antarctica, *J. Geophys. Res.*, *105*(D19), 24,491–24,508.

Mosley-Thompson, E., J. R. McConnell, R. C. Bales, Z. Li, P.-N. Lin, K. Steffen, L. G. Thompson, R. Edwards, and D. Bathke (2001), Local to regional-scale variability of Greenland accumulation from PARCA cores, *J. Geophys. Res.*, *106*(D24), 33,839–33,851.

Mote, T. L. (2003), Estimation of runoff rates, mass balance, and elevation changes on the Greenland ice sheet from passive microwave observations, *J. Geophys. Res.*, *108*(D2), 4056, doi:10.1029/2001JD002032.

Murphy, B. F., I. Marsiat, and P. Valdes (2002), Atmospheric contributions to the surface mass balance of Greenland in the HadAM3 atmospheric model, *J. Geophys. Res.*, *107*(D21), 4556, doi:10.1029/2001JD000389.

Ohmura, A., and N. Reeh (1991), New precipitation and accumulation maps for Greenland, *J. Glaciol.*, *37*(125), 140–148.

Ohmura, A., M. Wild, and L. Bengtsson (1996), A possible change in mass balance of Greenland and Antarctic ice sheets in the coming century, *J. Clim.*, *9*, 2124–2135.

Ohmura, A., P. Calanca, M. Wild, and M. Anklin (1999), Precipitation, accumulation, and mass balance of the Greenland ice sheet, *Z. Gletscherkd. Glazialgeol.*, *35*(1), 1–20.

Pfeffer, W. T., M. F. Meier, and T. H. Illangasekare (1991), Retention of Greenland runoff by refreezing: Implications for projected future sea-level change, *J. Geophys. Res.*, *96*(C12), 22,117–22,124.

Pinto, J. O., J. A. Curry, A. H. Lynch, and P. O. G. Persson (1999), Modeling clouds and radiation for the November 1997 period of SHEBA using a column climate model, *J. Geophys. Res.*, *104*(D6), 6661–6678.

Pomeroy, J. W., and R. Essery (1999), Turbulent fluxes during blowing-snow: Field tests of model sublimation predictions, *Hydrol. Processes*, *13*, 2963–2975.

Putnins, P. (1970), The climate of Greenland, in *Climates of the Polar Regions*, *World Surv. of Climatol.*, vol. 12, edited by S. Orvig, pp. 3–112, Elsevier Sci., New York.

Reeh, N., C. Mayer, H. Miller, H. H. Thomson, and A. Weidick (1999), Present and past climate control on fjord glaciations in Greenland: Implications for IRD-deposition in the sea, *Geophys. Res. Lett.*, *26*, 1039–1042.

Rignot, E. J., S. P. Gogineni, W. B. Krabill, and S. Ekholm (1997), North and northeast Greenland ice discharge from satellite radar interferometry, *Science*, *276*, 934–937.

Schmidt, R. A. (1982), Properties of blowing-snow, *Rev. Geophys.*, *20*, 39–44.

Steffen, K., and J. E. Box (2001), Surface climatology of the Greenland ice sheet: Greenland Climate Network 1995–1999, *J. Geophys. Res.*, *106*(D24), 33,951–33,964.

Steffen, K., and T. DeMaria (1996), Surface energy fluxes of Arctic winter sea ice in Barrow Strait, *J. Appl. Meteorol.*, *35*, 2067–2079.

Sturm, M., J. Holmgren, M. König, and K. Morris (1997), The thermal conductivity of seasonal snow, *J. Glaciol.*, *43*(143), 26–41.

Tabler, R. D. (1991), Snow transport as a function of wind speed and height, in *Cold Regions Engineering: Proceedings, Cold Regions Sixth International Specialty Conference*, pp. 729–738, Tech. Counc. on Comput. in Civ. Eng., Am. Soc. of Civ. Eng., Reston, Va.

Thomas, R. H., and PARCA Investigators (2001), PARCA 2001, Program for Arctic Regional Climate Assessment (PARCA): Goals, key findings, and future directions, *J. Geophys. Res.*, *106*(D24), 33,691–33,706.

Thompson, S. L., and D. Pollard (1997), Greenland and Antarctic mass balances for present and doubled atmospheric CO_2 from the GENESIS version-2 global climate model, *J. Clim.*, *10*, 871–900.

Troen, I., and L. Mahrt (1986), A simple model of the atmospheric boundary layer: Sensitivity to surface evaporation, *Boundary Layer Meteorol.*, *37*, 129–148.

Turner, J., T. A. Lachlan-Cope, G. J. Marshall, E. M. Morris, R. Mulvaney, and W. Winter (2002), Spatial variability of Antarctic Peninsula net surface mass balance, *J. Geophys. Res.*, *107*(D13), 4173, doi:10.1029/2001JD000755.

van der Veen, C. J. (2002), Polar ice sheets and global sea level: How well can we predict the future?, *Global Planet. Change*, *32*, 165–194.

van de Wal, R. S. W., M. Wild, and J. R. de Wolde (2001), Short-term volume changes of the Greenland ice sheet in response to doubled CO_2 conditions, *Tellus, Ser. B*, *53*, 94–102.

van Lipzig, N. P. M., E. van Meijgaard, and J. Oerlemans (1999), Evaluation of a regional atmospheric model using measurements of surface heat exchange processes from a site in Antarctica, *Mon. Weather Rev.*, *127*, 1994–2011.

Warren, S. G. (1982), Optical properties of snow, *Rev. Geophys.*, *20*, 67–89.

Wendler, G., C. Stearns, G. Weidner, G. Dargaud, and T. Parish (1997), On the extraordinary winds of Adélie Land, *J. Geophys. Res.*, *102*(D4), 4463–4474.

Wild, M., and A. Ohmura (2000), Changes in mass balance of the polar ice sheets and sea level under greenhouse warming as projected in high resolution GCM simulations, *Ann. Glaciol.*, *30*, 197–203.

Wild, M., P. Calanca, S. C. Scherrer, and A. Ohmura (2003), Effects of polar ice sheets on global sea level in high-resolution greenhouse scenarios, *J. Geophys. Res.*, *108*(D5), 4165, doi:10.1029/2002JD002451.

Zuo, Z., and J. Oerlemans (1997), Contribution of glacier melt to sea level rise since AD 1865: A regionally differentiated calculation, *Clim. Dyn.*, *13*, 835–845.

Zwally, H. J., and M. B. Giovinetto (2000), Spatial distribution of surface mass balance on Greenland, *Ann. Glaciol.*, *31*, 126–132.

Zwally, H. J., and M. B. Giovinetto (2001), Balance mass flux and ice velocity across the equilibrium line in drainage systems of Greenland, *J. Geophys. Res.*, *106*(D24), 33,717–33,728.

Zwally, H. J., W. Abdalati, T. Herring, K. Larson, J. Saba, and K. Steffen (2002), Surface melt-induced acceleration of Greenland ice-sheet flow, *Science*, *297*, 218–222.

L.-S. Bai, J. E. Box, and D. H. Bromwich, Polar Meteorology Group, Byrd Polar Research Center, Ohio State University, 1090 Carmack Road, Scott Hall Room 108, Columbus, OH 43210-1002, USA. (box.11@osu.edu)